Fakultät für Physik und Astronomie

Ruprecht-Karls-Universität Heidelberg

Diplomarbeit
im Studiengang Physik
vorgelegt von

Stefan Sellner

aus Mannheim

2010

# Echtzeit-Bildgebung der Annihilationsvertexverteilungen für in biologischen Zielen stoppende Antiprotonen

Die Diplomarbeit wurde von Stefan Sellner

ausgeführt am

Max-Planck-Institut für Kernphysik

unter der Betreuung von

Herrn Prof. Joachim Ullrich

Department of Physics and Astronomy

University of Heidelberg

Diploma thesis
in Physics
submitted by

Stefan Sellner

born in Mannheim

2010

# Real-Time Imaging of the Annihilation Vertex Distributions for Antiprotons Stopping in Biological Targets

This diploma thesis has been carried out by Stefan Sellner

at the Max Planck Institute for Nuclear Physics

under the supervision of

Prof. Joachim Ullrich

## Kurzfassung

Krebs ist in Deutschland die zweithäufigste Todesursache. Zu seiner Bekämpfung wurden verschiedenste Methoden entwickelt, wovon eine die Bestrahlung des Tumorgewebes mit geladenen Teilchen darstellt. Ihre schädliche Wirkung lässt sich zwar prinzipiell sehr gut auf das Tumorgewebe begrenzen, jedoch ist dazu die genaue Kenntnis der Gewebezusammensetzung, die sich im Teilchenstrahl befindet, nötig, weil davon die Reichweite des Strahls abhängt. Diese Zusammensetzung ist jedoch nicht sehr genau messbar, ferner wird sie durch Fehlpositionierungen und Bewegungen des Patienten während der Bestrahlung beeinflusst. Um dadurch entstehende Fehler in der Bestrahlung, die entweder den Tumor nicht vollständig abtöten oder gesundes Gewebe verletzen, zu vermeiden, ist ein Verfahren nötig, das die Reichweite des Strahls in Echtzeit messen kann. Die bislang einzig verfügbare Technik zur Verifikation der Behandlung kann diese jedoch nicht Echtzeit bestimmen. In dieser Arbeit wird auf eine Methode eingegangen, welche die bei einer Bestrahlung mit Antiprotonen emittierten Sekundärteilchen mit einem relativ einfachen Detektoraufbau misst, um aus deren Flugrichtungen Rückschlüsse auf die Annihilationsvertexverteilung im bestrahlten Gewebe zu ziehen. Die Anwendbarkeit dieser Methode wird in dieser Arbeit experimentell bestätigt und es werden Vergleiche mit Simulationen angestellt.

## Abstract

Cancer constitutes the second largest fraction of lethal illnesses in Germany. Several methods for its cure have been developed, one of which is the irradiation of the tumor tissue with charged particles. Their deleterious effect can in principle be limited to the tumor tissue, but a precise knowledge of the tissue composition along the particle beam is needed. This composition can, however, not be measured with high precision, and is further influenced by a possible misalignment as well as the movement of the patient. To avoid errors in the irradiation which could lead either to a non-complete tumor destruction or to damage introduced to healthy tissue, a method that is capable of determining the particle range in real-time is desirable. The only one used so far for quality assurance is not able to provide information in real-time. In this thesis, a technique is described that measures the secondary particles created upon irradiation with antiprotons with a rather simple detector set-up, and uses the direction of flight information to reconstruct the annihilation vertex distribution in the irradiated tissue. The applicability of this technique is verified in this thesis and compared to simulations.

# Contents

# 1 Introduction

## 1.1 Cancer

Cancer (malignant neoplasm) is a group of diseases where cells grow uncontrolled, invade or destroy neighboring tissue, or spread to other places in the body. This unlimited growth can either lead to a benign or a malignant tumor. Benign tumors grow in a controlled way, and do not invade other tissues, e.g. moles. Malignant tumors can spread to distant locations (metastasize) and become life threatening. The medical branch of oncology deals with all aspects of cancer like diagnosis, treatment and prevention.

The World Health Organization (WHO) estimated that cancer accounted for 7.6 million or 13 % of all deaths worldwide in 2004 [WHO09]. In Germany, cancer makes up the second largest fraction of reasons for death (cf. figure 1.1). In principle, every organ can be seized

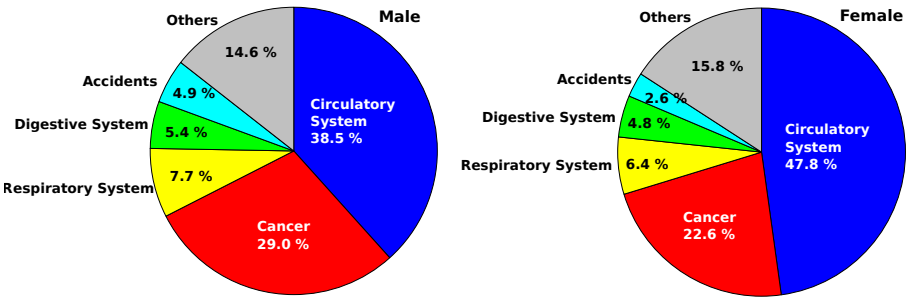


**Figure 1.1:** The most frequent causes of death in Germany 2007. Data taken from [BN98]

by cancer, and the risk of developing cancer strongly depends on age, gender, eating habits and particularly on the presence of carcinogens, like tobacco smoke, radiation or viruses. Sometimes the increased risk of cancer can be inherited, if certain genes controlling the DNA replication are broken or disabled.

Cancer cells show typically two peculiarities: on the one hand cancer-promoting genes are activated and enable the cell to grow in an uncontrolled way, not obeying the cell death program, which should be executed if the cell notices that something went irreparably wrong. On the other hand, the inactivated tumor suppressor genes result in the loss of the normal function of the cell, especially in the proper interaction with protective cells of the immune system.

First diagnosis of cancer is usually triggered by the occurrence of symptoms or by observing irregularities in radiographic images. Definitive diagnosis can be obtained by the histological examination of a small sample of the tissue of interest. In most cases, cancer can be treated and often even cured. The success however strongly depends on its type, location and stage. Usually a combination of surgery, chemotherapy and radiotherapy is applied as treatment.

## 1.2 Benefits and challenges of conformal radiotherapy

The two ultimate goals of cancer therapy are to maximize the tumor control probability (TCP) and to minimize the normal tissue complication probability (NTCP). In radiation therapy, this can be achieved by focusing the deposited energy as precisely as possible on the tumor or by adding radio-sensitizing drugs to the tumor tissue. The basic relation between TCP and NTCP is illustrated in figure 1.2. The tumor control probability is represented by the red curve, the normal tissue complication probability by the green one. Of course, shape and distance between the two curves depend on many factors, such as tumor type, radiation type, the condition of the patient etc. The distance between the curves at 50 % level is called the therapeutic window. In this region, good tumor control can be achieved without causing much damage to healthy tissue or nearby organs at risk. Its maximization is the goal of recent research. The wider the therapeutic window is, the higher the achievable tumor control is before normal tissue effects negate the benefits of the treatment. As an example, a better treatment method could result in the dashed green line, where the normal tissue complication probability is moved to higher doses and the therapeutic window (blue dashed line) is enlarged. As will be described in chapter 2 in more detail, the use of particle irradiation instead of photon irradiation enables a better dose conformity possible and allows a higher dose delivered to the tumor compared

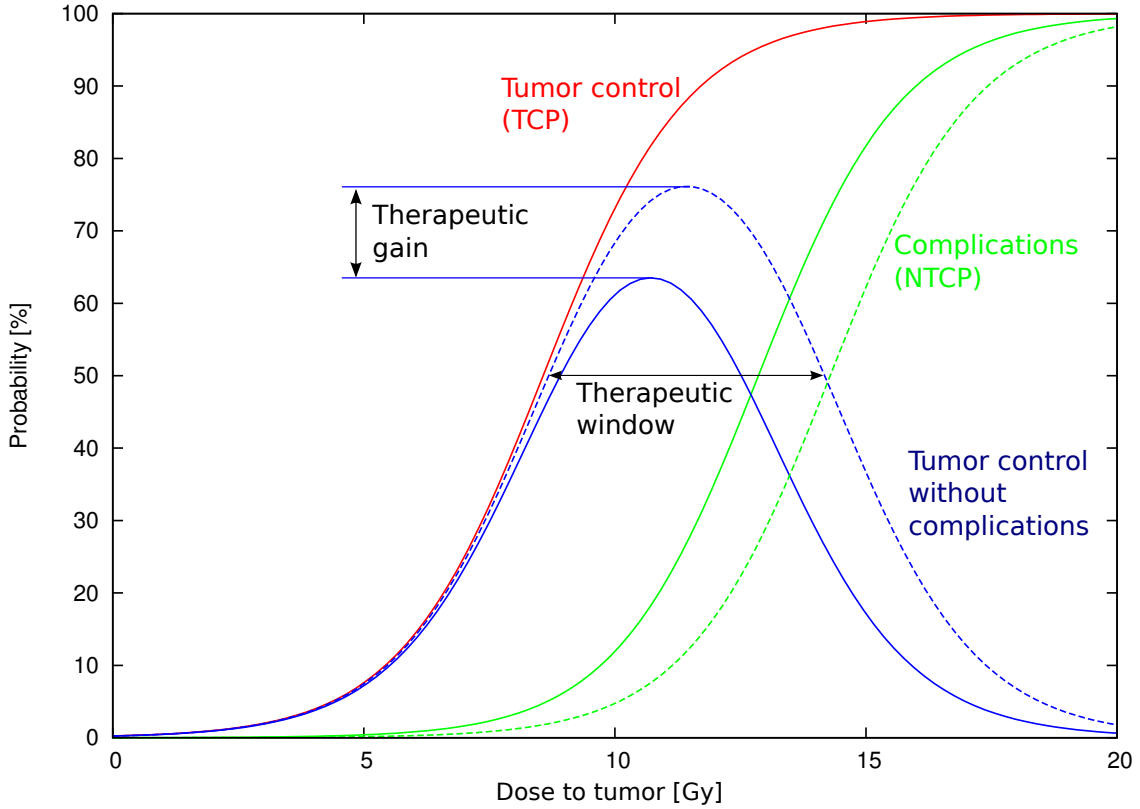


**Figure 1.2:** Basic relation between TCP, NTCP and the therapeutic window

to the surrounding tissue, which in turn increases the therapeutic window. However, such a gain in treatment effectiveness needs a precisely optimized treatment plan which again requires input data of high quality. In most cases, CT images are the basis for the delineation of the tumor boundaries and the determination of the tissue composition along the planned irradiation direction. The latter is, however, only possible within certain error ranges, as the conversion of the x-ray absorption into material distributions is not precise. Furthermore, the stopping powers (cf. chapter 2) of the elements themselves are not known precisely enough. Not only the physical input data introduces uncertainties, but also any changes e.g. of the position of the patient during the course of the treatment. K. Parodi et al. have shown that even small geometrical deviations of the patient during the treatment and the treatment plan, e.g. because of misalignments or physiological changes, can introduce a severe degradation of the dose delivered in terms of homogeneity and shape [Par08].

To detect and correct for such deviations, it is highly desirable to be able to monitor in real-time the treatment process to avoid that harm is unintentionally introduced to healthy tissue and assure that the exact prescribed dose is delivered to the entire target. Applying a too high dose to normal tissue or nearby healthy organs can lead to severe side effects, but missing a portion of the tumor will simply lead to failure of the treatment.

Up to now, however, no such method has been developed.

And this is where this thesis begins. In chapter 2, the basics of radiation therapy are briefly summarized. Chapter 3 is about the experiment carried out at CERN, and the methods used for data analysis. Results are presented in chapter 4, and discussed and compared to Monte-Carlo simulations in chapter 5. Chapter 6 concludes the thesis and gives an outlook to further experiments.

# 2 Basics

In this chapter, a brief summary of the historical development of radiotherapy is given and basic physical and radiobiological quantities and concepts underlying radiation therapy of cancer will be introduced.

## 2.1 Positions

The frequently used names for relative positions with respect to the "reference" point, like distal, proximal and lateral are illustrated in figure 2.1.

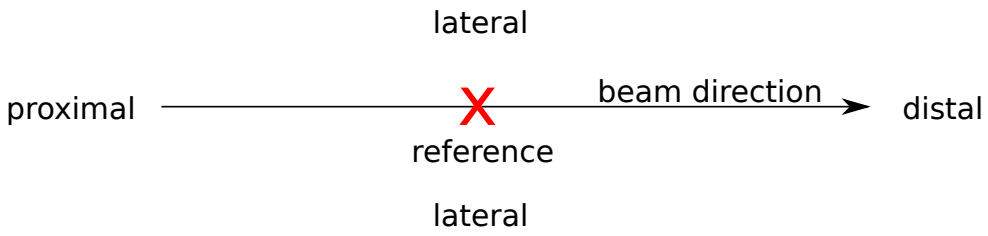


**Figure 2.1:** Directions

## 2.2 Radiotherapy: historic context

The therapeutic use of ionizing radiation goes back to 1896, when Leopold Freund, an Austrian surgeon, used x-rays to treat a hairy mole, making it disappear [Fre97]. These x-rays were discovered only one year earlier by W.C. Röntgen [Rön95]. The first cancer treatments using x-rays were carried out by Grubbe, Despeignes, Williams and Voigt. From then on, radiation therapy developed in a fairly empirical way with two general tendencies:

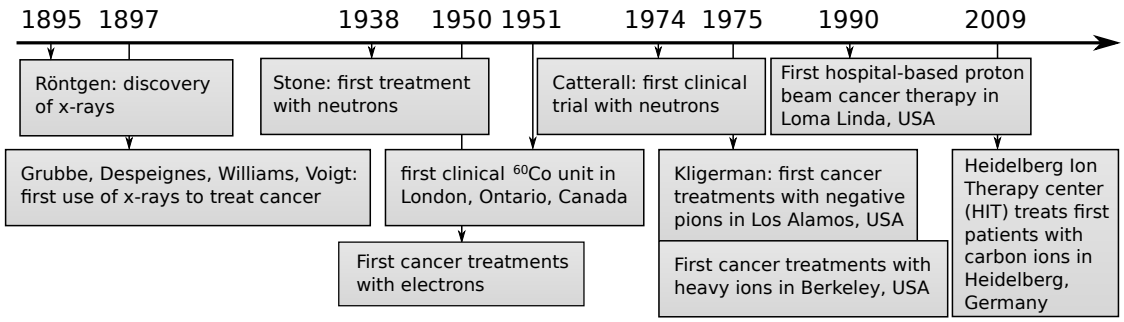


**Figure 2.2:** Milestones in cancer irradiation therapy. Part of data taken from [Hal06]

- Increased radiation dose conformity, either increasing the dose (for a definition, see next paragraph) to the tumor while leaving the dose to the surrounding tissue unchanged, or decreasing the dose to the surrounding tissue at an unchanged tumor dose.
- Increased biological effect of the used radiation (cf. section 2.3).

As the absorption of ionizing electromagnetic radiation is a stochastic process and can therefore be described by an exponential law, the ratio of radiation damage to healthy tissue in front of a deep seated tumor to the tumor itself is larger than one, which means that more harm is done to the healthy tissue compared to the tumor. By changing the radiation source to $^{60}$Co and thus, increasing the energy of the radiation, the peak dose could be shifted further inside the tissue which is especially beneficial to the very radiation sensitive skin. The physical explanation is given in section 2.6.1. Modern radiation therapy uses high-energy electron bremsstrahlung typically up to $20\,\mathrm{MeV}$ generated by a linear accelerator, which shifts the peak dose further into the target, as described in section 2.6.1. An even higher dose conformity can be achieved by irradiating under many different angles, building up a high dose in the overlap region while leaving the average dose to healthy tissue low, and by applying intensity modulation techniques to produce complicated 3D shapes of the high dose target area. Nevertheless, the total dose delivered outside the target remains high and presents a growing concern with respect to secondary cancer in long term survivors.

To increase the biological effect of radiation to tissue, other radiation types than photons were examined, for example electrons, neutrons and pions. Especially pions were expected to have beneficial properties since they can undergo nuclear reactions and thus, deposit

additional energy. In clinical trials this benefit could however not be demonstrated. Neutrons have a higher biological effectiveness but a long range, so that normal tissue is harmed significantly, resulting in severe late effects. Electrons in the megavolt energy range are well applicable to treat superficial tumors (less than 5 cm deep). Compared to photons of the same energy, their depth dose curve exhibits a higher surface dose, but a steep decrease at the end of the electron range with a tail due to bremsstrahlung.

Robert Wilson was the first who examined the depth dose properties of heavy charged particles, such as protons [Wil46]. Their steep increase in ionization density and dose towards the end of their range had already been observed for alpha particles by Bragg 1903 [Bra05]. This is why the maximum of the depth dose curve is also called Bragg peak. A more thorough description of the physical properties is given later. The facts that the dose before the tumor is lower than the dose at the tumor with practically no dose being deposited distal, i.e. behind the Bragg peak along with the small lateral scattering of heavy charged particles as compared to electrons makes them an ideal candidate for the treatment of deep-seated tumors.

Heavier ions have an even higher ionization density than protons, and especially for carbon ions the increase of this ionization density essentially coincides with the increase of physical dose in the Bragg peak. This results in a higher relative biological effectiveness (for a definition, see next section) in the target volume which has been shown by Kraft et al. and makes carbon ions a valuable tool to treat deep-seated radiation resistant tumors [Kra00]. The quest for further increase of the biological effective dose in the tumor region lead Kalogeroupolos et al. to suggest antiprotons as irradiation particles as they deposit additional energy when they annihilate at the end of their range and part of this additional energy is deposited in form of particles with high ionization density [Kal89].

## 2.3 Basic quantities

**Dose** is the amount of energy $E$ transferred by ionizing radiation to an object with the mass $m$: $D = \frac{E}{m}$ and has the unit 1 Gray (Gy) = 1 $\frac{J}{kg}$. In radiation therapy of cancer, typical doses to treat tumors are in the range of $20 - 80\,\mathrm{Gy}$ delivered in $1 - 2\,\mathrm{Gy}$ fractions per day. Compared to everyday's life energy measures, one Gray is a rather small quantity: a full body dose of $10\,\mathrm{Gy}$ is lethal with 90 % probability (LD90), but would heat the body

by only $0.0024\,°\mathrm{C}$. The reason why this small amount of energy still is so powerful lies in the nature of the energy absorption. Its general important characteristics is the very localized release of this energy in a cascade of ionization reactions following the primary ionization events: The average energy released per single ionization in this cascade is in the range of $30\,\mathrm{eV}$, enough to break chemical bonds which have binding energies typically less than $10\,\mathrm{eV}$. Photons for example, with typical treatment energies ($2 - 20\,\mathrm{MeV}$) lose their energy mainly by a series of inelastic Compton scattering and pair production reactions (cf. figure 2.3).

**Stopping power** is the average amount of energy lost per unit path length by fast particles due to ionization of the surrounding material:

$$S = \frac{dE}{dx}$$

In some cases, the mass stopping power $S/\rho$ is used with $\rho = dm/dV$, ($m$: mass, $V$: volume). The stopping power can be divided into three independent contributions: the electronic or collision stopping power, which is dominant for heavy charged particles, the radiative stopping power due to bremsstrahlung (only relevant for electrons), and the nuclear stopping power due to elastic Coulomb scattering (negligible for particle energies above 1 MeV):

$$S = -\left[\left(\frac{dE}{dx}\right)_{electronic} + \left(\frac{dE}{dx}\right)_{radiative} + \left(\frac{dE}{dx}\right)_{nuclear}\right]$$

The dominating electronic part can be described by the Bethe [Bet30] formula (the high-energy, relativistic correction term has been omitted):

$$S = -\frac{dE}{dx} = 2\pi N_A r_e^2 m_e c^2 \rho \frac{Z}{A}\frac{z_{eff}^2}{\beta^2}\left[ln\left(\frac{2m_e\gamma^2 v^2 W_{max}}{I^2}\right) - 2\beta^2\right]$$

($N_A$: Avogadro's Number, $r_e$: classical electron radius, $m_e$: electron mass, $c$: speed of light, $\rho$: target material density, $Z$: target material charge, $A$: target material atomic number, $z_{eff}$: effective charge of the projectile (see below for further details), $\beta = v/c$, $\gamma = 1/\sqrt{1 - v^2/c^2}$, $v$: projectile velocity, $W_{max}$: maximum energy transfer by a single collision, $I$: mean excitation potential of the target material, can be approximated by $I = 11.5 \cdot Z$)

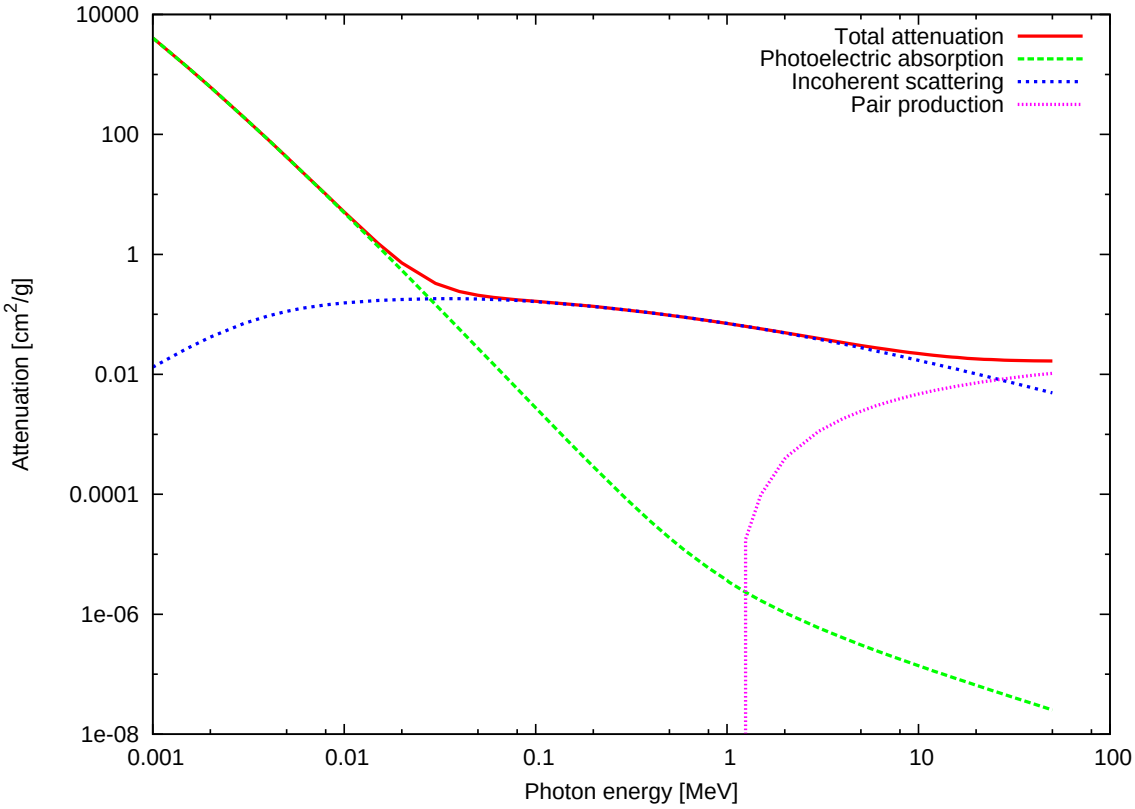


**Figure 2.3:** Photon attenuation curves for water. Data taken from [Ber98]

The effective projectile charge $z_{eff}$ depends on the particle's velocity. At high energies (> 10 MeV/u, u: atomic mass unit with $1u = 1/12\ m_{^{12}C}$), the projectiles are fully ionized. As the projectile slows down, it collects more and more electrons, which decreases the effective charge and would result in a longer range. However, the velocity $\beta$ also decreases and approaches zero which, because it appears in the denominator, results in a high loss rate of the residual particle energy and a decrease of the remaining range. Important for treatment purposes are the dependencies of the energy loss from the projectile (its effective charge $z_{eff}^2$ and velocity $\beta^2$) and the tissue ($\rho$, $Z$, $A$, and $I$). The logarithmic term changes only slowly.

All effects that become relevant for particle energies of $1-10\,\mathrm{MeV}$, e.g. the Barkas effect:

$$z_{eff} = z\left[1 - \exp^{-125\beta Z^{-2/3}}\right]$$

or resonant electron capture, are irrelevant for therapy purposes, as the remaining range of the ions at these energies is only a few millimeters. Further discussion is done later in section 2.6.

**Linear energy transfer (LET)** is closely related to the stopping power and describes the amount of energy per unit path length transferred to the surrounding matter in terms of electrons produced in ionization events of the incident particle, so-called secondary electrons. Compared to the stopping power, it only refers to the energy deposited by secondary electrons that have a kinetic energy smaller than the threshold energy $\Delta$, and thus, the energy deposited in the vicinity of the projectile's track.

$$LET_\Delta = \frac{dE_\Delta}{dx}$$

$dE_\Delta$ is the energy loss due to electronic collisions minus the kinetic energies of all secondary electrons with an energy larger than $\Delta$. The latter is not a constant physical quantity, but is chosen to fit to the experiment in question, e.g. by the thickness of a detector or the size of a cell. A frequently chosen value for $\Delta$ is $10\,\mathrm{keV}$, corresponding to a secondary electron range of a few millimeters, which is the typical electrode spacing in ionization chambers. As the most likely secondary electron energy for typical primary particle energies is around $1\,\mathrm{keV}$, most electrons are accounted for. The LET of photon irradiation is rather low ($0.3\,\mathrm{keV}/\mu\mathrm{m}$ for $3\,\mathrm{MeV}$ photon energy) compared to the LET of particle irradiation (about ten $\mathrm{keV}/\mu\mathrm{m}$ for $1-10\,\mathrm{MeV}$ protons and several tens to more than $200\,\mathrm{keV}/\mu\mathrm{m}$ for carbon ions at energies between $10$ and $100\,\mathrm{MeV/u}$, respectively).

**Surviving fraction** $S$. As radiation therapy is dealing with living organisms, quantities measuring the biological effect are necessary. In the case of in-vitro cell cultures, the surviving fraction is easily accessible by counting the number of cells that survived an exposure to a certain irradiation dose. The surviving fraction can be parameterized with good accuracy by the linear-quadratic model [Lea46]:

$$S = S_0 \exp^{-\left(\alpha D + \beta D^2\right)}$$

$S_0$: number of cells before irradiation, $\alpha$, $\beta$ radiation and tissue parameters, $D$ dose.

In models for a theoretical interpretation of the induced damage, the factor $\alpha D$ can be understood as a probability for a DNA double-strand brake caused by a single ionization

event and $\beta D^2$ can be understood as probability for two DNA single-strand brakes in tight temporal and spacial vicinity. In both cases, the DNA damage is likely to be irreparable, causing the cell to call its apoptosis (suicide) program.

**Relative biological effectiveness (RBE).** The linear-quadratic model holds for sparsely ionizing (low-LET) radiation, e.g. x-rays, as well as densely ionizing (high-LET) particles. As the biological effect depends not only on the dose, but also on the particle type and energy through its physical interaction mechanism with matter, the concept of the relative biological effectiveness has been introduced to relate the biological effect of particle irradiation to the one of photon irradiation. It is defined as the ratio between the dose delivered by $^{60}$Co x-rays and the dose of the irradiation in question, achieving the same biological effect, e.g. a specific surviving fraction of 1 %:

$$RBE_{1\,\%} = \left.\frac{D_{x-ray}}{D_{particle}}\right|_{1\,\%}$$

A graphical illustration is shown in figure 2.4.

The RBE depends on many different physical quantities, such as LET, dose, dose rate (dose per time), particle type, and particle energy. It increases with the linear energy transfer up

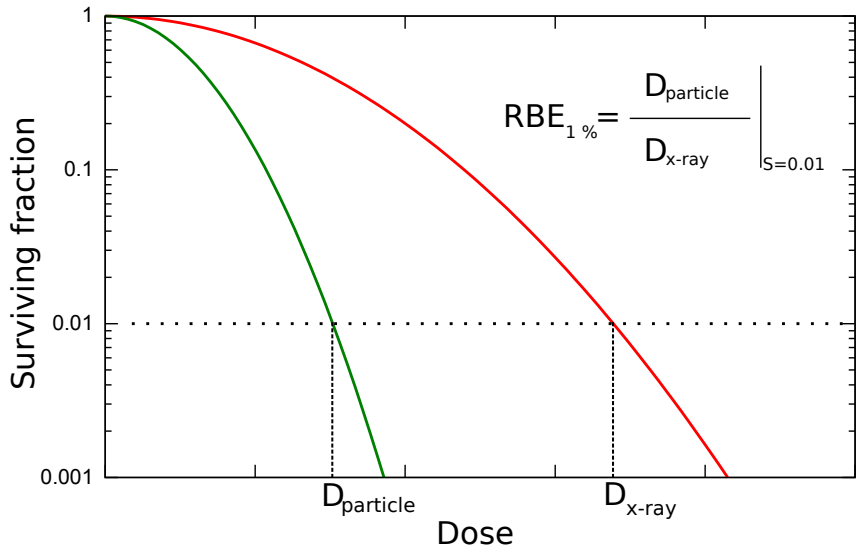


**Figure 2.4:** Definition of RBE$_{1\,\%}$

to a maximum and decreases again afterwards (see figure 2.5). The reason is cell overkill, meaning that the probability of a cell death has approached unity and cannot increase further. The LET where the RBE reaches its maximum depends on the particle type. It is about $25\,\mathrm{keV}/\mu\mathrm{m}$ for protons and about $200\,\mathrm{keV}/\mu\mathrm{m}$ for carbon ions.

For living organisms, the survival fraction of cells is not accessible. Therefore, the RBE and other radiobiological quantities are defined as the ratio of doses reaching the same probability of an effect, e.g. paralysis in mice or tumor growth, to occur. The RBE is further complicated by the fact that it also depends on biological issues like cell line, tissue type, oxygenation of cells, etc. There are several models that try to predict the RBE from physical quantities, such as the local effect model (LEM) [Sch94].

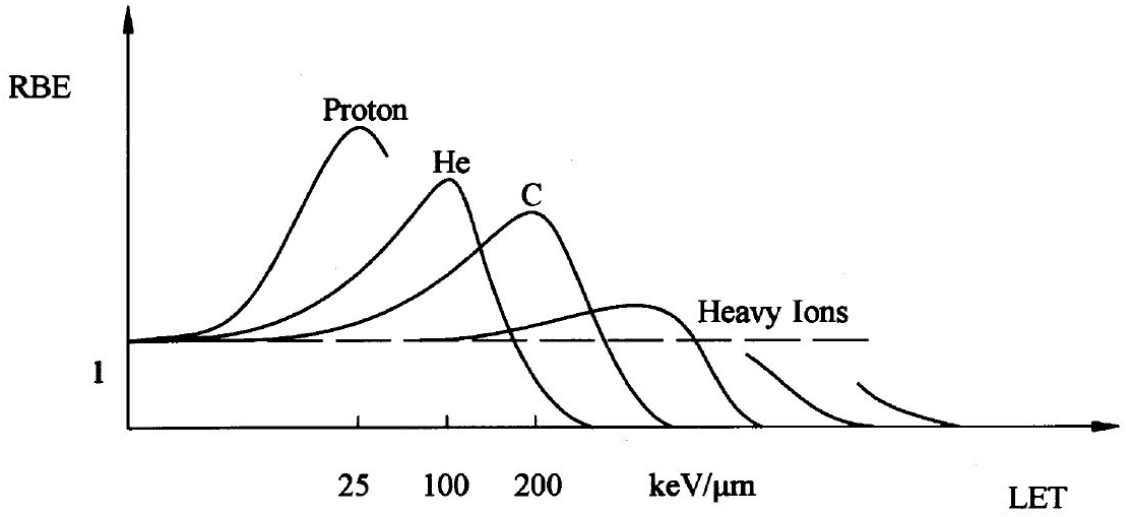


**Figure 2.5:** LET dependancy of the RBE for different particles

## 2.4 Present status of particle irradiation imaging

As already pointed out in section 1.2, many factors have an impact on the accuracy of cancer treatment with particles, and a real-time treatment monitoring is desirable. The only method which is successfully used as a quality assurance method is PET (positron emission tomography) imaging. It makes use of the fact that the beam particles can initiate nuclear reactions, producing $\beta^+$ emitters with a certain probability. When a $\beta^+$ emitter decays, it emits a positron which annihilates with an electron, producing in two or three photons, depending on the positronium state. In the case of para-positronium ($^1\mathrm{S}_0$) the most probable decay channel is the emission of two photons that escape back-to-back because of momentum and energy conservation. The coincident impact of these photons into a detector is used to back-calculate the position of the annihilating positron, and, thus the position of the $\beta^+$ emitter, which in turn is related to the position of the particle beam. For protons as irradiation particles, the oxygen nuclei in the target tissue can be transformed into the $\beta^+$ emitters $^{15}\mathrm{O}$ with a half-life of about $2$ minutes. As these nuclear reactions require energies between $5$ and $20\ \mathrm{MeV}$ of the incident protons [Gue97], the distribution of the created $\beta^+$ emitters varies along the depth as the protons lose more and more energy with increasing penetration length. For carbon ions as irradiation particles, not only the target tissue nuclei can be activated, but also the beam particles themselves by stripping one or two neutrons, resulting in the $\beta^+$ emitters $^{10}\mathrm{C}$ and $^{11}\mathrm{C}$ with half-lives of about $20$ seconds and about $20$ minutes, respectively [Nat]. For a typical beam energy used in treatments (about $90\,\mathrm{MeV/u} - 430\,\mathrm{MeV/u}$), up to 80 % of the carbon ions become activated, which have a slightly longer range because of their decreased mass. In any way, the expected $\beta^+$ activity is located along the beam direction, with a maximum at the end of the range of the incident ions. To detect a reasonable signal, a certain amount of activity has to be built up first. Therefore, at current intensities, the PET method is only applicable inter-fractional, i.e. after completion of an irradiation fraction.

For the quality assurance, the treatment plan is used to simulate the expected PET activity distribution. After irradiation, the patient's PET distribution is measured and finally compared to the calculated distribution (cf. figure 2.6). If there is no large deviation in terms of range and width of the measured distribution, the treatment is considered to have succeeded. If there is a significant deviation, the most recent irradiation is considered to have failed and changes are applied to the treatment plan. Thus, the patient has been

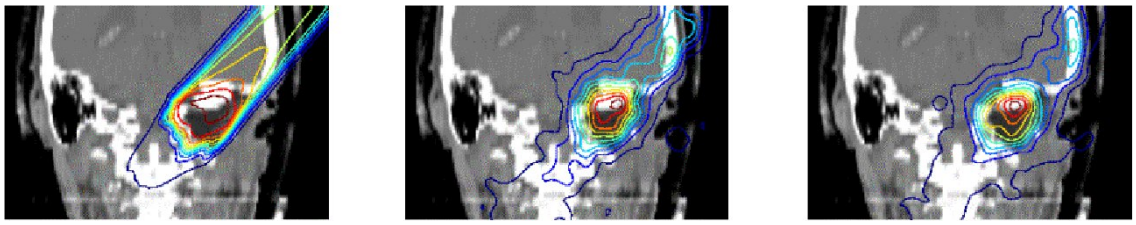

**Figure 2.6:** PET irradiation verification. Left: treatment plan, center: simulated PET response, right: measured PET response

irradiated wrongly for a portion of the treatment, which contradicts the goal of minimizing the normal tissue complication probability.

A promising approach towards real-time imaging during treatment under development is to detect prompt gamma radiation released after nuclear fragmentation events (cf. figure 2.7).

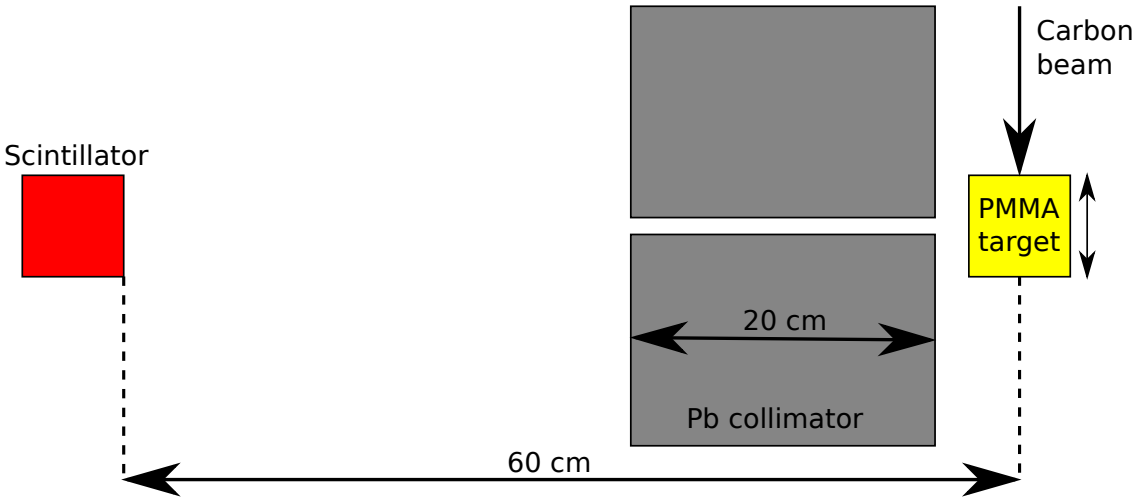


**Figure 2.7:** Setup for the prompt gamma radiation measurement. Picture taken from [Tes09]

Testa et al. irradiated a PMMA target with $73\,\mathrm{MeV/u}$ carbon ions provided at the GANIL facility [Tes09]. A time-of-flight set-up with a scintillating detector behind a lead collimator discriminated the photons created upon fragmentation of the carbon ions with a spectrum that reaches up to $20\,\mathrm{MeV}$ from other background particles, mainly neutrons. Because of the collimator only photons coming from a narrow depth range are observed in the

scintillator and the depth dose profile can be measured by shifting the collimator in axial direction. Under realistic irradiation conditions, this profile could be measured in real-time with an accuracy of about $1\,\mathrm{mm}$. However, with the used set-up the signal to background ratio is only in the range of $3$ and furthermore it is not possible to reconstruct the full two-dimensional dose distribution at once.

## 2.5 AD-4/ACE

The AD-4/ACE (Antiproton Cell Experiment) collaboration at the European Organization for Nuclear Research (CERN) (cf. figure 2.8) examines the properties of antiprotons as irradiation particles.

Compared to the commonly known LHC experiments it is extremely small and located at the Antiproton Decelerator (AD) [Bai97], where other experiments investigate fundamental properties of antimatter, especially of antihydrogen.

### 2.5.1 Antiproton production

The AD runs parasitically to the LHC and is supplied with protons accelerated by the Proton Synchrotron (PS), which is the source of protons for the LHC. The PS is capable to provide protons, electrons, positrons and heavy ions to various experiments within a supercycle of up to $43$ seconds. One pulse of protons at $26\,\mathrm{GeV/c}$ is extracted every $90$ seconds to an iridium target where the high kinetic energy of the incident protons is partly transformed into antiprotons with a broad momentum spectrum (see figure 2.9). As the maximum antiproton yield at the primary proton momentum used is around $3.2\,\mathrm{GeV/c}$, antiprotons around this momentum are captured from the target by a magnetic horn and injected into the AD. The AD then decelerates and cools them in several stages using stochastic and electron cooling. The lowest momentum available from the AD is $105\,\mathrm{MeV/c}$ ($5\,\mathrm{MeV}$ kinetic energy), which is used by the most of the other experiments currently installed at the AD. To obtain a penetration depth of about $10\,\mathrm{cm}$ of the antiprotons in tissue, as desired for our experiment the energy is only decreased to $127\,\mathrm{MeV}$ ($500\,\mathrm{MeV/c}$).

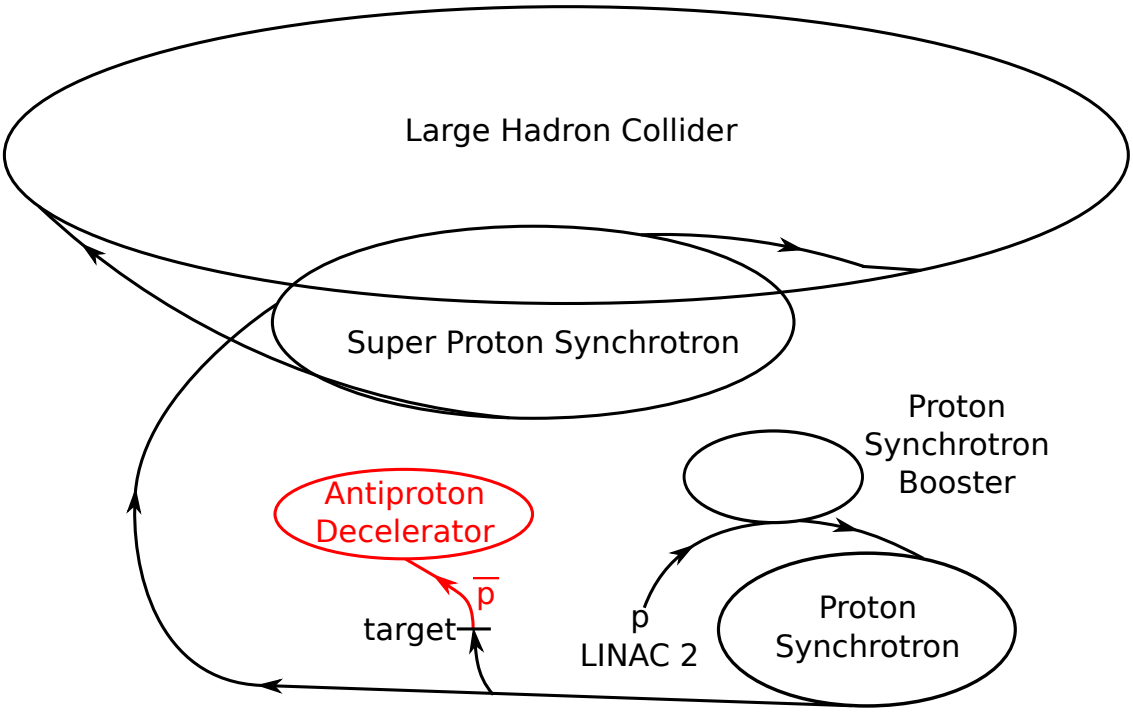


**Figure 2.8:** A part of CERN's accelerator complex. The Antiproton Decelerator is drawn in red

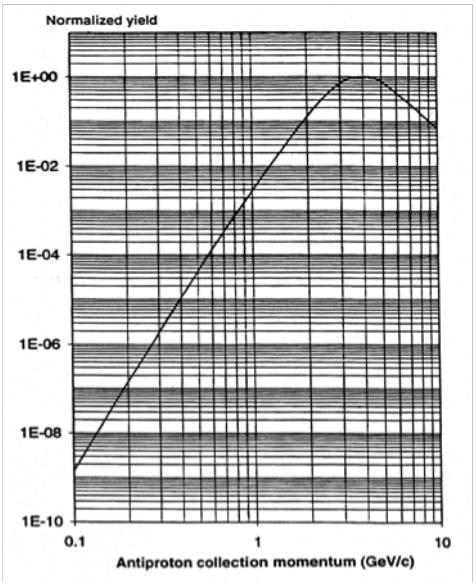


**Figure 2.9:** Antiproton momentum spectrum for an initial proton momentum of $26\,\mathrm{GeV/c}$

## 2.6 Irradiation Therapy

In this section, a short comparison between different methods used in irradiation therapy is provided.

### 2.6.1 Photon irradiation

The uncharged photons transfer energy to surrounding matter indirectly by photoionization, Compton scattering and pair production. The hereby released secondary electrons transfer their energy to the tissue. The energy-dependent cross sections for these three mechanisms have been plotted in figure 2.3. As photons are uncharged, the interaction is stochastic and the energy deposition can be described by an exponential decay, as can be seen in figure 2.10 for the $100\,\mathrm{keV}$ photons. They are sparsely ionizing. For higher energetic photons, the electrons created have higher energies and a range of centimeters. As the density of air is much smaller than the density of water, significantly less secondary electrons are created in air compared to water. Together with the different electron energies this results in a non-equilibrium electron density and energy distribution at the boundary from air to water at $0\,\mathrm{cm}$. The dose at small depth is therefore smaller than at deeper depths, until the equilibrium is reached. This phenomenon is called build-up effect and is beneficial for treatment as the skin situated in the first centimeter is very sensitive to radiation. For photon energies of $20\,\mathrm{MeV}$, the dose maximum is shifted to about $7\,\mathrm{cm}$. As soon as the equilibrium is reached, the dose is decaying exponentially again.

The overall shape of the curves shows that the amount of deposited energy does not change much along the depth, meaning that healthy tissue in front of and behind a deep-seated tumor is exposed to a high dose. That is why typical tumor irradiation is done from many different sides and angles. Then, the dose to the tumor is added up by the doses delivered from each angle, whereas healthy surrounding tissue receives a low dose. However, the volume of irradiated healthy tissue and the integral dose applied to the patient is high.

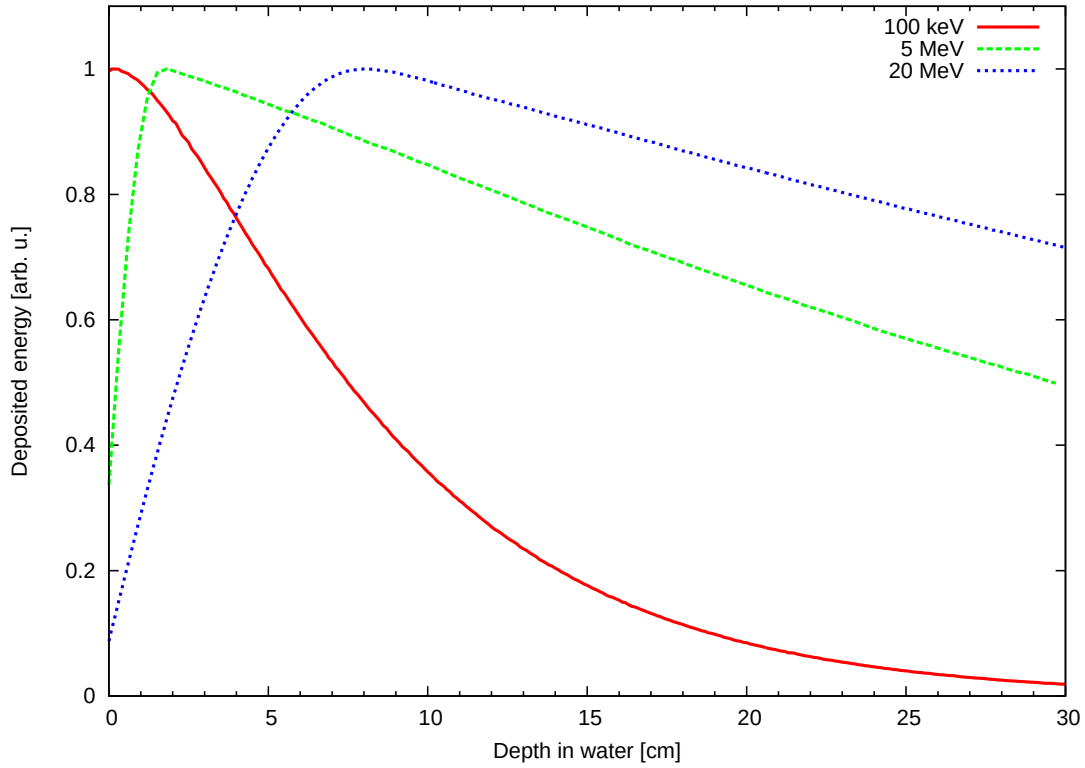


**Figure 2.10:** Depth dose curves for photons of different energies, normalized to their maximum

### 2.6.2 Particle irradiation

Charged particles "see" the charged constituents of the surrounding matter and interact with them, different to the stochastic interaction of photons. Compared to photons, they are densely ionizing for typical treatment energies (about $50\,\mathrm{MeV} - 220\,\mathrm{MeV}$ for protons, about $90\,\mathrm{MeV/u} - 430\,\mathrm{MeV}$ for carbon ions), with a quadratic increase of ionization density with their charge. The continuous energy loss (also called continuous slowing down) due to ionizations and excitations decreases the kinetic energy of the particles, resulting in a stopping at a certain depth, depending on the incident energy. As described by the Bethe formula in section 2.3, the amount of deposited energy is low for high particle energies and is highest at very low energies, resulting in a so-called Bragg peak of delivered dose, as can be seen in figure 2.12, where the dose is plotted for protons, carbon ions and antiprotons.

### 2.6.3 Antiprotons

The depth dose curve for antiprotons looks similar to the curve for protons, especially for smaller depths as the electromagnetic interaction with the surrounding water is the same for the same charge state (cf. figure 2.12). However, as the antiprotons are antiparticles to the surrounding protons, they annihilate mostly at the bragg peak, where they come to rest. There, an additional amount of energy of twice the proton mass, $2\,\mathrm{M_p c^2} = 1.88\ \mathrm{GeV}$ is released.

In terms of usefulness in tumor treatment applications, the particles created upon an antiproton annihilation event can be classified into the "good", the "bad", and the "ugly" ones (figure 2.11).

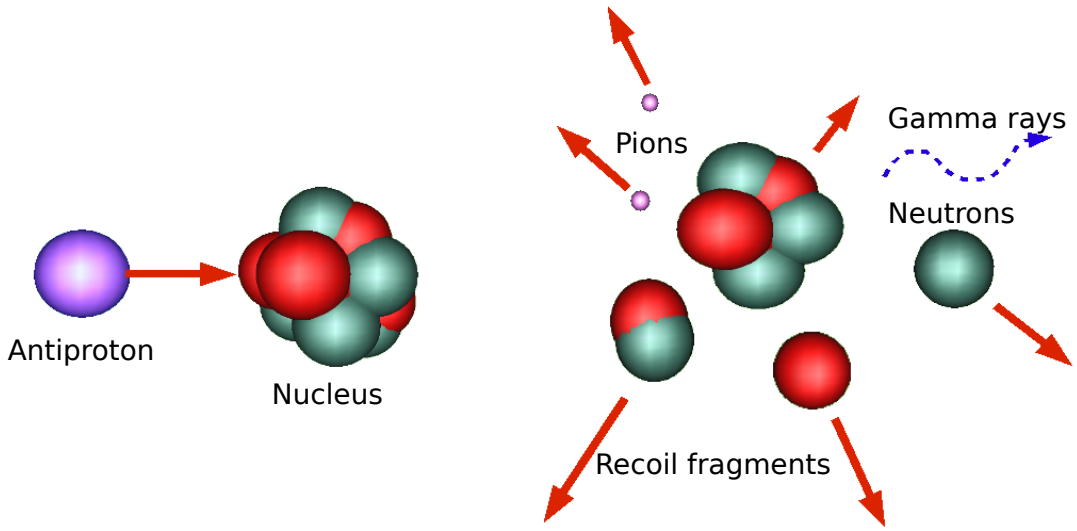


**Figure 2.11:** Antiproton annihilation event

- The good: the recoiling fragments of the hit nuclei have a high ionization density and a short range. Sullivan compared the energy deposition of protons and antiprotons and estimated that about additional $30\,\mathrm{MeV}$ are released directly within a few millimeters around the annihilation vertex [Sul85].
- The bad: the dominant process is the pion production because of the quark structure

of protons and antiprotons [Ino89]:

$$\overline{p} + p \rightarrow \pi^+ \, \pi^- \, \pi^0$$

Because of kinematics, the mean number of created pions is four. After subtraction of the rest mass energy of the four pions, about $1.24\,\mathrm{GeV}$ kinetic energy is shared by them, yielding an average kinetic energy of about $300\,\mathrm{MeV}$ per pion. The charged pions decay after about $2.6 \times 10^{-8}\,\mathrm{s}$, enough to propagate through long distances, causing a whole-body ambient dose (cf. the tail behind the Bragg peak for antiprotons in figure 2.12), fortunately, with a low ionization density. The uncharged pion $\pi^0$ decays after only $0.8 \times 10^{-16}\,\mathrm{s}$ into mostly two high-energy photons which hardly interact with the surrounding matter. On the other hand, the charged pions enable a real-time supervision of the two-dimensional annihilation distribution by measuring their direction of flight and reconstruction of the annihilation vertices.

- The ugly: neutrons are also created. They have a long range and a high ionization density along with a high RBE.

Initial measurements reported an enhancement by a factor of $4$ for the biological equivalent dose ratio (BEDR) for antiprotons compared to protons for nearly identical initial conditions [Hol06]. The next step was to measure the absolute applied dose by alanine pellets and ionization chambers and to compare the results to computer simulations. With that, the physical dose deposited in the Bragg peak was assessed to be twice the dose deposited by protons for an identical dose deposition in the entrance channel, with an additional increase of the relative biological effectiveness by another factor of about $2$ due to the high LET components in the annihilation [Bas08a], [Bas08c].

However, the concern was raised that some of the secondary particles created in the annihilations have a long range and cause a higher ambient dose compared to protons outside the target area. Whether this aspect would cancel the benefit of the increased dose in the Bragg peak is one of our group's present research [Fah09].

### Comparison of different particle species

All depth dose curves in figure 2.12 are normalized to the dose in the entrance channel, i.e. at $0.5\,\mathrm{cm}$ depth and do not contain information about the biological effectiveness. After the stopping of the particles, no dose can be deposited at larger depths by the incident particles, but some background dose due to secondary particles still exists and will be different for different primary particles.

While the overall shapes of the depth dose curves for different heavy charged particles are similar, there are significant differences between the dose deposition patterns for different particles. Protons are the lightest possible charged ions. Virtually no dose is deposited after their stopping point which is beneficial for the tissue behind the targeted tumor tissue. The depth of the stopping point depends on the initial proton energy and is about $15\,\mathrm{cm}$ for $127\,\mathrm{MeV}$ protons. However, protons and antiprotons show considerable lateral scattering because of their small mass. This lateral scattering is much reduced for the heavier carbon ions, but because they are compound nuclei, they undergo fragmentation along their path. The lighter fragments have a longer range than the incident ions, which produces the dose tail after the stopping depth of the unfragmented particles. Also secondary neutrons produced by nuclear interactions along the flight path are strongly forward peaked. However, the relative biological effectiveness of carbon ions is about three in the Bragg peak, meaning that obtaining the same biological effect, the number of carbon ions can be decreased to about a third. Thus, the dose in the entrance channel and in the tail distal to the Bragg peak is significantly reduced. The relative biological effectiveness of protons can be well approximated as $1.1$ over the whole range, for the one of antiprotons the same argument holds as for the carbon ions: the RBE is about two in the peak region, meaning that the number of antiprotons can be decreased, which results in an even lower entrance dose. However, the volume exposed to low doses is always highest for antiprotons due to the secondary particles created upon annihilation events with a long range.

For the simulation of a treatment of an extended tumor volume, N. Bassler et al. changed the range and intensities of the beam particles and weighted them differently such that the tumor volume recieves a homogeneous high dose [Bas10]. Here, the characteristics of the particle species become more pronounced, as shown in figures 2.13–2.15. An irradiation of a $4 \times 4 \times 4\ \mathrm{cm}^3$ target was optimized in terms of target coverage and dose to non-target volume. Comparing the physical dose distributions for protons and antiprotons,

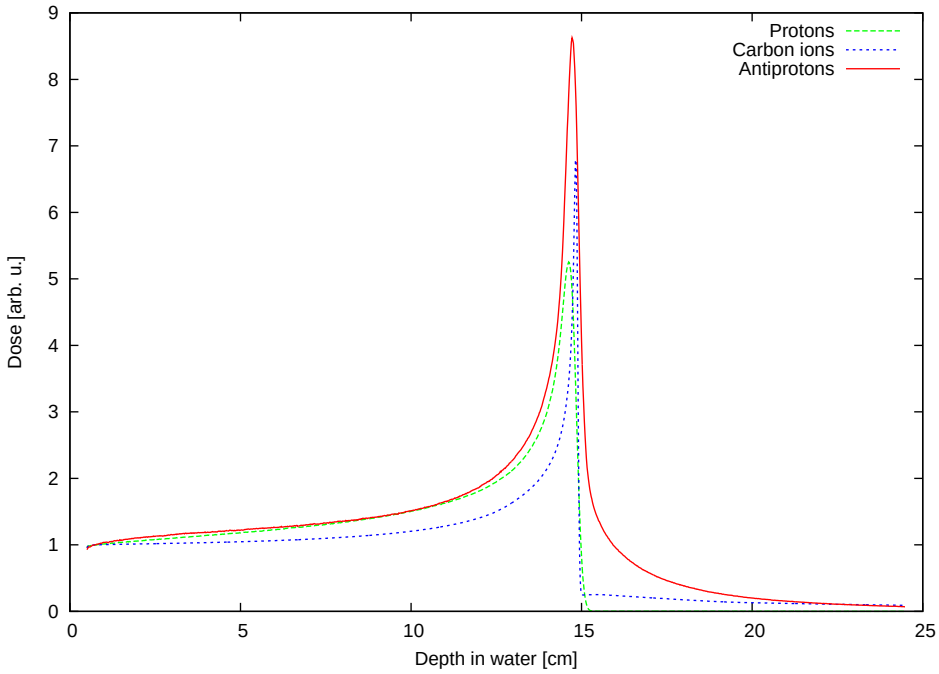


**Figure 2.12:** One-dimensional depth dose curves for protons, carbon ions and antiprotons

it can be clearly seen that the dose in the entrance channel is significantly decreased. The drawback of antiprotons is, however, the low ambient dose in the whole volume. For carbon ions, the lateral precision is higher due to the lower lateral scattering. The dose in the entrance channel is higher than both in the proton and antiproton case, and a low-dose tail behind the target volume is present. However, as mentioned above, the RBE has not been taken into account, which reduces the biological effective entrance channel doses for both antiprotons and carbon ions.

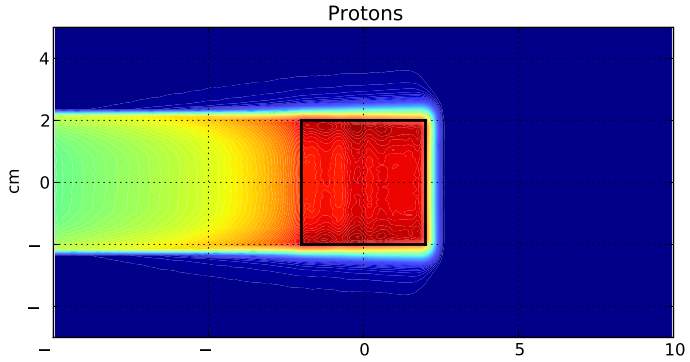


**Figure 2.13:** Treatment plan for protons

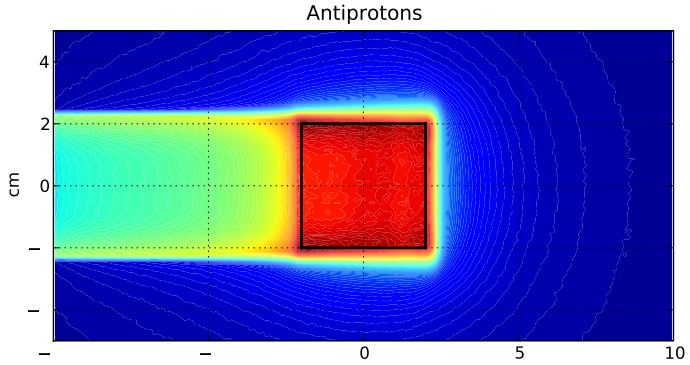


**Figure 2.14:** Treatment plan for antiprotons

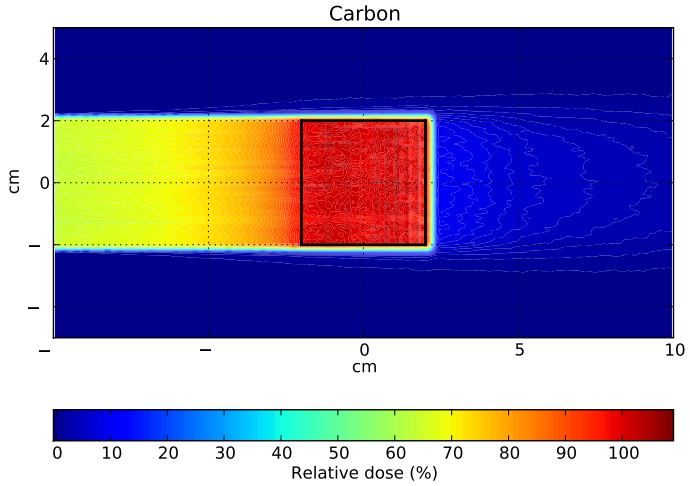


**Figure 2.15:** Treatment plan for carbon ions

# 3 Materials and Methods

## 3.1 Motivation

Pions generated in antiproton annihilations (cf. section 2.6.3) can be used for tomography of the annihilation distribution [Fuj04]. I. Kantemiris has shown in simulations under realistic irradiation conditions that these pions are numerous enough to obtain the depth dose distribution in real-time [Kan10]. He simulated the irradiation of a $4 \times 4 \times 4\,\mathrm{cm}^3$ target in a $20 \times 20 \times 20\,\mathrm{cm}^3$ water phantom with antiprotons and observed the escaping charged pions using a typical high energy physics detector setup: it consists of four detectors with three layers of sensitive planes, each with high granularity (pixel size is $100\,\mu\mathrm{m}$), covering $30\,\%$ of the solid angle (cf. figure 3.1).

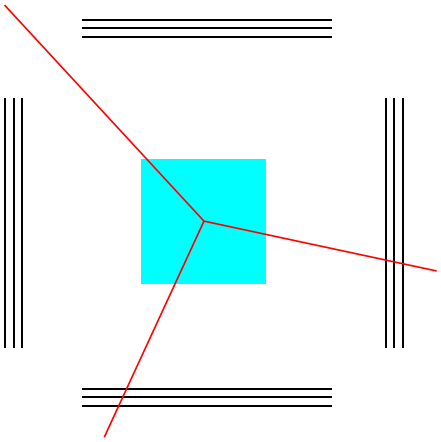

**Figure 3.1:** Virtual detector setup from the beam eye's view. Blue: water phantom, black: detector planes, red: pion tracks

With the assumption that each annihilation event can be discriminated in time, the idea is to backcalculate the tracks of the detected pions. If two reconstructed tracks approach each other within one millimeter or less, the center of the line connecting these tracks is considered as the annihilation vertex. About $25\,\%$ of the produced pions stop within the phantom, some undergo scattering, leading to the loss of information of their origin, and some do not cross the detector. This reduces the overall efficiency to about $1\,\%$. But for a physical dose of $2\,\mathrm{Gy}$ of antiprotons, about $2 \times 10^8$ pions cross the detector giving enough statistics to even reconstruct the distribution during the first fraction of the treatment (or potentially to reduce the size of the detector system). With this, he was able to reconstruct the delivered dose distribution by assessing the

annihilation vertex distribution from the pions' track information with a precision in the range of $1\,\mathrm{mm}$. By scoring not only pions, but all charged particles, only negligible noise is introduced, as shown in figure 3.2.

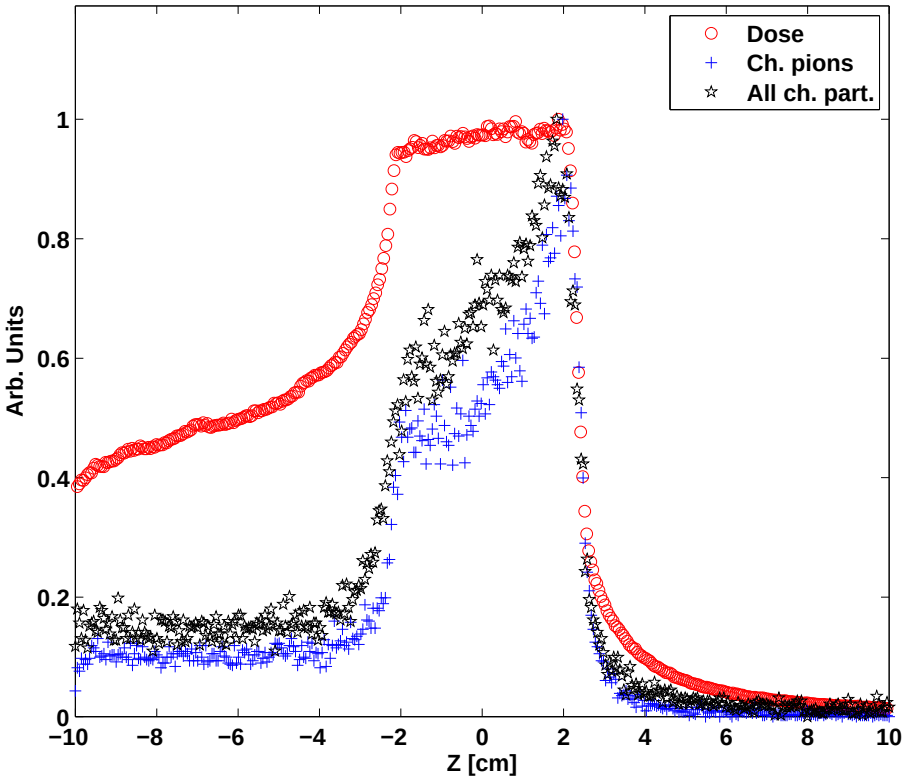


**Figure 3.2:** Comparison of vertex distributions obtained for pions only (crosses) and when all particles are included in the reconstruction (open stars). The depth dose is plotted with open circles. Image courtesy of I. Kantemiris [Kan10]

The goal of the experiment carried out within the framework of this thesis was to test the feasibility to use a simpler detector setup to image the annihilation vertex distribution, both for reasons of cost savings and open access for patient placement.

## 3.2 Set-up

The idea behind the simpler detector set-up is to use a silicon pixel detector (SPD) in a rather unconventional way. It is positioned such that the pions originating from antiproton

annihilation events transverse the detector under a grazing angle, leaving tracks of different lengths behind, depending on the exact angle of impact. The length of the tracks can be used to calculate the pion's origin, which gives access to the original one-dimensional antiproton annihilation vertex distribution. In this experiment, a spare silicon pixel detector [Rie03] that is originally forming a part of the vertex locator in the ALICE experiment [The99] at the LHC is used.

### Overview

The primary purpose of the AD-4/ACE-experiment is to determine the radiobiological properties of antiprotons as irradiation particles. An overview of the set-up is drawn in figure 3.3. Biological cell samples are stored in a gel to prevent them from moving and filled into a tube which is inserted into the beam axis. In order to halt the cell metabolism during the long irradiation times needed due to the AD beam intensity and time structure, the tube is cooled to $4\,^{\circ}\mathrm{C}$ in a bath consisting of a mixture of water and glycerine. The ratio of the two liquids is chosen to match the density $\rho = 1.04\,\mathrm{g/cm^3}$ of the gel and the tube to simulates the presence of normal surrounding tissue in a typical treatment scenario, leading to dose equilibration by backscattering.

To produce a spread-out Bragg peak, several thin PMMA (polymethylmethacrylate) sheets can be inserted into this section to decrease the energy of the antiprotons before entering the water phantom. Typically, measurements by the AD-4 collaboration are carried out using a $1 - 2\,\mathrm{cm}$ flat-top Bragg peak. After accounting for materials like the entrance window to the target tank, the distal edge of the Bragg peak is found about $10\,\mathrm{cm}$ deep into the water bath.

In the beam diagnostics section, several tools are used to measure the properties of the antiproton pulses. A beam current monitor capable of integrating pulses with rise times as short as picoseconds is used to determine the current and thus the number of antiprotons in each pulse. A scintillating foil which is filmed by a CCD camera can also be used to get an estimate of the beam shape and intensity. Radiochromic dosimetry films are used to determine the beam shape, to detect deviations of the beam position, and to assess its geometrical properties, such as eccentricity and FWHM. Except for the beam current monitor, however, all devices need several pulses to deliver a reasonably strong

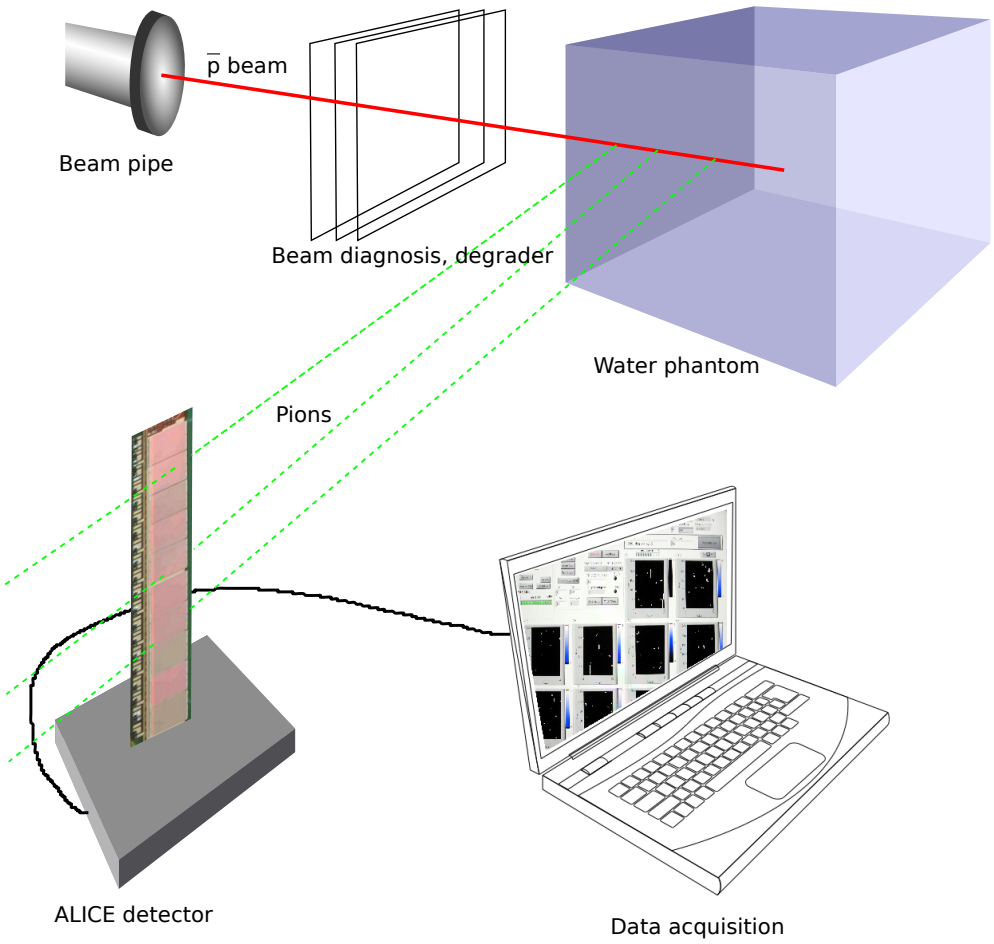


**Figure 3.3:** Simplified real-time imanging set-up

signal. To overcome this, a beam position and profile monitor based on a monolithic silicon pixel detector is currently in preparation. First measurements carried out at the beam time in September 2009 showed that the detector is capable to cope with the enormous instantaneous intensities of antiprotons in a pulse, delivering all the desired beam parameters for each pulse.

The real-time imaging detector set-up is placed at a $1.4\,\mathrm{m}$ distance to the beam axis and runs parasitically during the whole irradiation process.

## Detector properties

The ALICE Silicon Pixel Detector (SPD) is the innermost part of the inner tracking system (ITS) of the ALICE experiment [The99]. Several of these detectors are mounted to two concentric barrels and are used for particle tracking. Because of the tracking purpose, the detector is optimised to only detect the presence of a transversing particle, but does not measure other parameters such as the number of created electron/hole pairs, for example, which could give an estimate of the particle's energy. The detector is built as a mixed signal hybrid consisting of a sensor and a read-out chip which is connected to the sensor with bump bonds. The hybrid structure allows the detector to run with low noise and power consumption. Each chip is fabricated in $0.25\,\mu\mathrm{m}$ technology with a radiation-tolerant design and has $256 \times 32$ pixels with the dimensions $50\,\mu\mathrm{m} \times 425\,\mu\mathrm{m} \times 200\,\mu\mathrm{m}$. Ten of such chips make up a half-stave, which has thus the dimensions $1.28\,\mathrm{cm} \times 13.6\,\mathrm{cm} \times 0.02\,\mathrm{cm}$ (figure 3.4). One such half-stave has been provided to us by the ALICE SPD group, including electronic read-out modules and software.

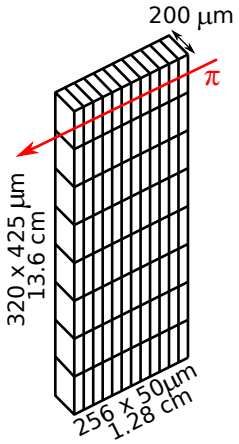


**Figure 3.4:** ALICE SPD dimensions. Red arrow: direction of flight of the pions

Each pixel has an analog and a digital part (cf. figure 3.5). In the analog part, the signal is amplified and shaped to a pseudo-Gaussian. In the discriminator, its height is compared to a threshold which can be set by a 3-bit number. It is also possible to apply a test pulse to the chip (C_test in the figure) for testing purposes. Dead or malfunctioning pixels can be disabled using the mask switch. The digital part contains a synchronizer and delay units to

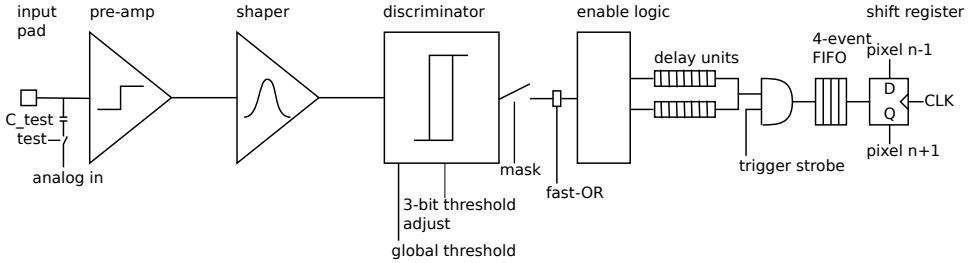


**Figure 3.5:** The signal processing within a pixel in the ALICE SPD detector. Drawing adapted from [Wyl99]

store the data until an eventual trigger pulse is received. If an external trigger is enabled and coincides with the delay unit output, a logic one is saved to the FIFO (first in, first out) buffer. For reading out the chip, the FIFO data is put into a 256-bit shift register, one per column. All of the 32 columns are read out in parallel.

Measurements by Petra Riedler et al. have indicated that the minimum threshold is 1000 electrons rms, and that the mean noise is about 110 electrons rms [Rie03] for a $^{55}$Fe source. The designed threshold is however in the range between 1000 and 2900 electrons rms. A minimum ionizing particle transversing the detector produces about 80 electrons per micrometer, which is the most probable energy loss.

The detector itself was mounted on a table that is turnable to be able to point with its vertical edge towards different regions in the water phantom.

Because of the limited size of the 256-bit shift register, the maximum hit occupancy of the detector is about $8\,\%$, which makes the rather large distance necessary to decrease the solid angle of the detector. A rough estimate using the area of the front edge of the detector, and the average amount of 4 pions per annihilation (cf. section 2.6.3) gives the number $\mathrm{N_t}$ of expected tracks:

$$\mathrm{N_t} = \Omega \times \frac{\mathrm{N_{pions}}}{\overline{p}} \times \frac{\mathrm{N_{\overline{p}}}}{\mathrm{pulse}} = \frac{200\,\mu\mathrm{m} \times 13.6\,\mathrm{cm}}{4\pi \times (1.4\,\mathrm{m})^2} \times 4 \times 3 \times 10^7 \approx 130$$

Furthermore, the integration time window is set to the last part (approx. $100\,\mathrm{ns}$) of each pulse to decrease the number of tracks further.

The detector is read out with electronic equipment that has been used for its comissioning. Changing of parameters, displaying detector responses and data saving is done with a LabVIEW 7.1 front end.

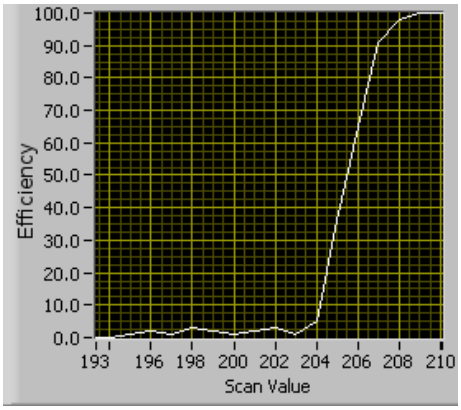


**Figure 3.6:** Screen shot of the chip averaged pixel response curve to different test pulses. Scan value: test pulse strength (proportional to the produced electron/hole pairs), efficiency: percentage of "hit" responses of a pixel

Using the LabVIEW front end, automatic routines were executed to determine and set the threshold value of each pixel by applying repeated test pulses of different strength via C_test (cf. figure 3.5) and measuring the pixel response (cf. figure 3.6). The threshold was set to the value where the pixel responded in $50\,\%$ of the test pulses. The result of the routine shows a mean average threshold which corresponds to an amount of $\mu(\mu_{pixel}) = 2400 \pm 240$ electrons per pixel.

For the orientation in the original ALICE set-up, the minimum ionizing particles traverse the detector along its $200\,\mu\mathrm{m}$ edge, producing $200\,\mu\mathrm{m} \times 80\,\mathrm{e}^{-}/\mu\mathrm{m} = 16{,}000$ electrons. In the orientation used in this experiment, the particles transverse it along the $50\,\mu\mathrm{m}$ edge, producing only $50\,\mu\mathrm{m} \times 80\,\mathrm{e}^{-}/\mu\mathrm{m} = 4{,}000$ electrons. As the energy loss is a statistical process, which can be described with a Landau distribution, the actual number of electron-hole pairs can be smaller than the threshold. That explains why the measured data shows gaps in the particle tracks as can be seen in the next chapter.

## 3.3 Raw data

Two example exposures are shown in figure 3.8. White pixels have been hit, black pixels have not. The exposures have been taken at two different detector angles (cf. figure 3.7), such that it was pointing towards the proximal part of the beam trajectory in the water

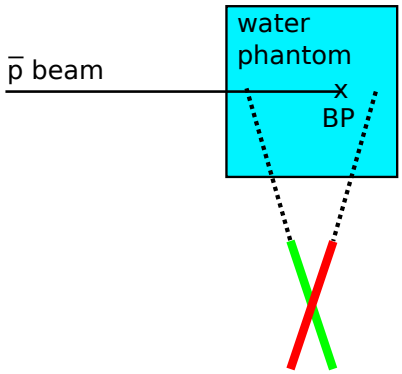


**Figure 3.7:** Schematic top-view drawing to illustrate the two detector angles. Green: proximal, red: distal, BP: Bragg peak

phantom (exposure in figure 3.8a), and slightly distal to the expected Bragg peak position, respectively (figure 3.8b). As expected, there are more short tracks in the proximal setting, resulting from the large amount of pions created in the Bragg peak region which leave short tracks behind. In the distal exposure, these pions create longer tracks. Of course, the distribution of the single exposures shows fluctuations in the number of tracks because the exposure window was set to capture only the last part of the antiproton pulse. Therefore, about 100 exposures were taken for each angle.

What can also be seen in figures 3.8a and 3.8b is that the tracks are often interrupted by gaps of different length. In the majority of cases, it is however intuitively possible to tell which parts of the interrupted lines form a track. The software implementation of this problem is described in the next section.

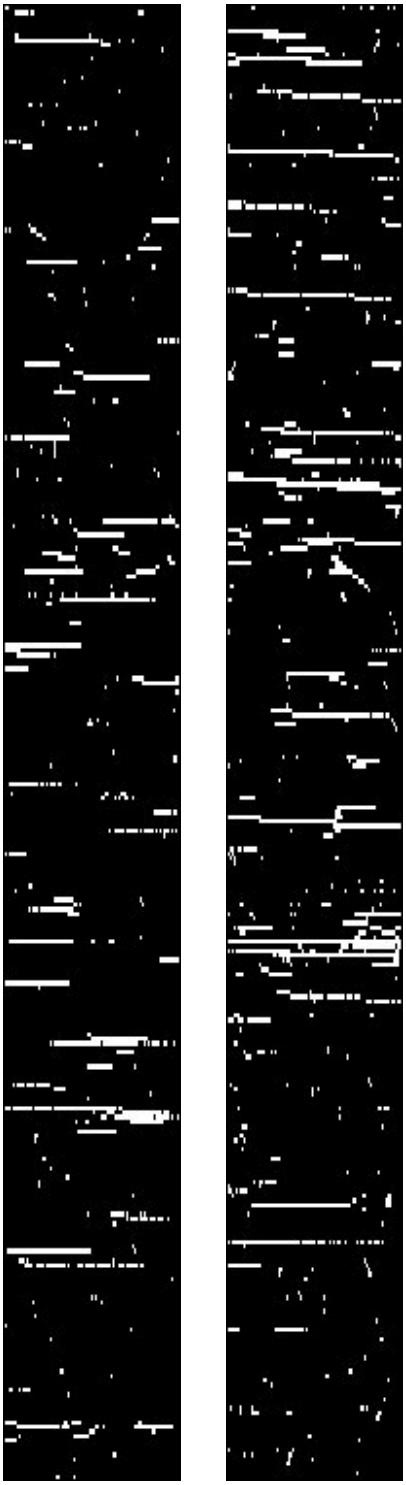

**(a)** proximal

**(b)** Bragg peak

**Figure 3.8:** Two raw data exposures

## 3.4 Processing algorithms

To reconstruct the annihilation vertex distribution, the lengths and coordinates of the tracks measured by the detector are the two important quantities that have to be extracted from the measurements. Thus, the next step of the data analysis is to find the coordinates of the endpoints of each track.

### 3.4.1 Hough transform

Initial attempts of data analysis were using an algorithm known in the field of image processing. The Hough transform [Hou62] is a feature extraction technique in image processing and can be used to find lines, and in a more general form, arbitrary shapes in pictures [Dud72]. The advantage of the transform is that the shapes do not have to be perfect as it finds them by a scoring technique. Therefore, it transforms the image into a parameter space. In the case of two-dimensional straight lines, the parameter space is as well two-dimensional as each point $(x_0, y_0)$ of the image space can also be regarded as an element of the straight line $y_0 = mx_0 + c$. The Hough method transforms this line to a parameter space generated by $m$ and $c$, e.g. $c = y_0 - mx_0$. For each hit pixel in the image space, this parameter pair is calculated and accumulated in the parameter space. The points lying on a straight line in the image space cause a local maximum of accumulated points in the parameter space. Thus, the next step after going through each point in the image space is to look for maxima in the parameter space. If a certain threshold is reached, a line which has the slope and intercept which caused the accumulation point is considered to be found. The version implemented and used in MATLAB can also detect vertical lines by transforming not to the parameter space $(m, c)$ as vertical lines would have $m = \infty$, but taking the distance of a point of the line to the origin and the angle with respect to the x-axis $(d, \alpha)$ as parameters. Another, not further documented routine can be used to find the endpoints of each line. However, the method seems to have great difficulties to detect the measured tracks with gaps, even though much effort was spent in finding suitable parameters for the algorithm like resolution, thresholds etc. Two examples are shown in figure 3.9. In figure 3.9a, loose parameters (e.g. grid size, threshold for local maxima in parameter space) were set, in figure 3.9b the parameters were more strict. In both samples

not all the tracks were detected, and those found are mostly too short and are detected multiply and with gaps.

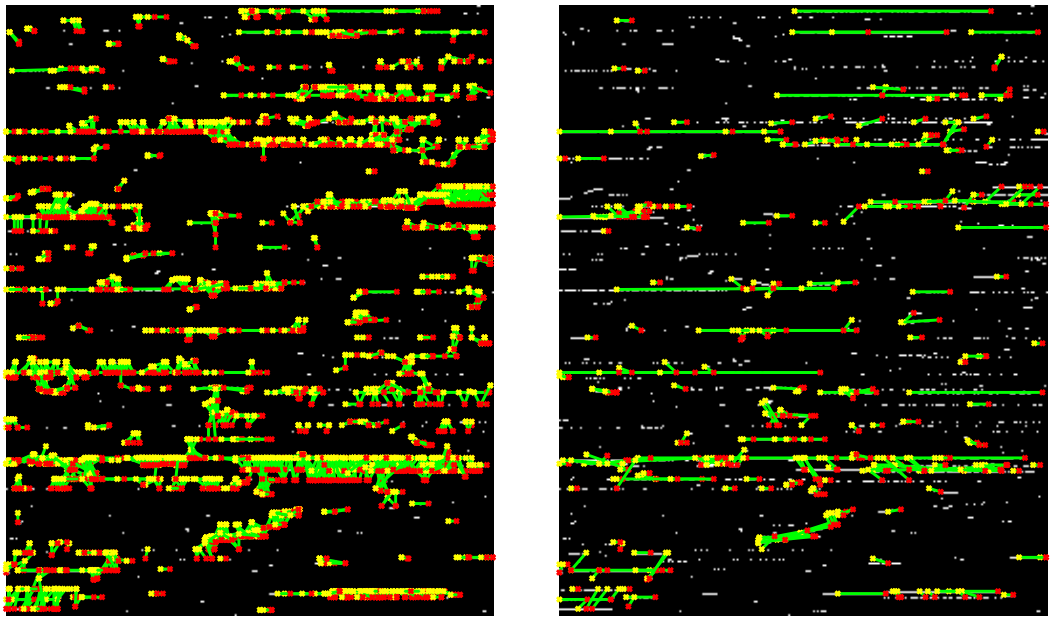

**(a)** **(b)**

**Figure 3.9:** Hough transform line fits

To overcome the problems with the Hough transform, the gaps are filled first using image morphology tools, and the lines are then detected with a more specialized code that takes into account that most tracks are horizontal.

### 3.4.2 Image morphology

To fix the gaps within the tracks, a modified *closing* operator, which consists of the two morphological operators *dilate* and *erode*, is used. In mathematical morphology, closing of a set $B$ using a structure element $S$ is the erosion of the dilation of $B$:

$$B \bullet S = (B \oplus S) \ominus S$$

$\oplus$ denotes the dilate operator, $\ominus$ the erode operator. Here, the set $B$ is the raw binary detector image and the structure element $S$ a horizontal line of 15 pixels length, matching

the gap lengths found in the raw data. The structure element was chosen to be horizontal because the vast majority of the tracks is completely horizontal. The principle of the dilate and erode operator is illustrated in figure 3.10 and 3.11. The structure element has a reference point as a probing pixel (black cross in the green and red bar in figures 3.10 and 3.11, respectively). The element is moved over the binary image pixel by pixel, such that the reference point overlays every pixel of the binary image. If the reference point overlays a hit pixel, then all the pixels under the structure element are switched on. On the other hand, if the pixel under the reference point is not hit originally, it is switched on if at least one pixel under the whole structure element, i.e. within a 7-pixel horizontal neighborhood is hit. By this, pixels in gaps are switched to hit pixels, if a pixel in the close horizontal neighborhood has been hit. A side effect that occurs is that also the pixels neighboring the endpoints of the tracks are switched on. This effect can, however, easily be corrected by applying the erode operator which is just the opposite of the dilate operator, as shown in figure 3.11.

Again, the pixel under the reference point of the structure element is switched off, if the area under the structure element is not completely switched on. This rule applies for all the pixels at the end of tracks. Because the gaps have been fixed before by the dilate operator, they are no more affected. Finally, the track length is reduced to the original length. However, single pixels close to the left and right margins are elongated by the dilate operator and not shortened again by the erode operator. To avoid artifacts, lines

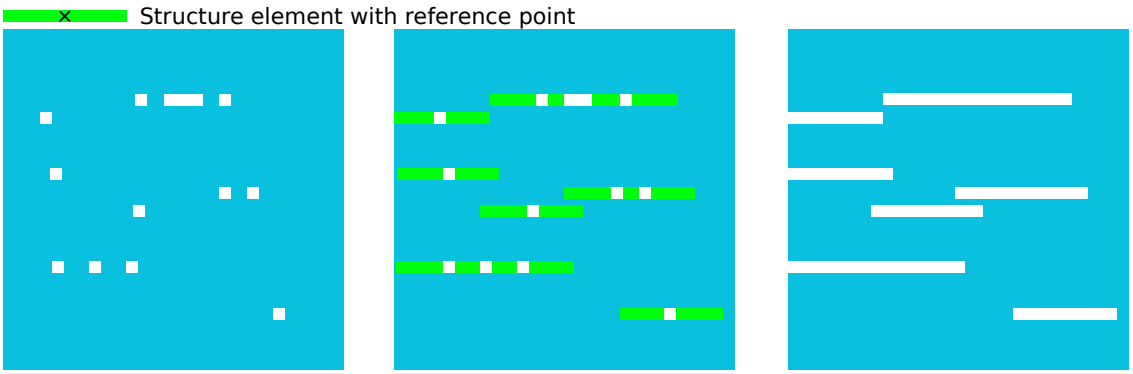


**Figure 3.10:** The dilate operator. Left: input raw image with gaps, white pixels are hit pixels. Center: after applying the dilate operator, the pixels changed to hit pixels are marked in green. Right: processed dilated image, the gaps have been fixed, but the lines are elongated. This image is further processed by the erode operator

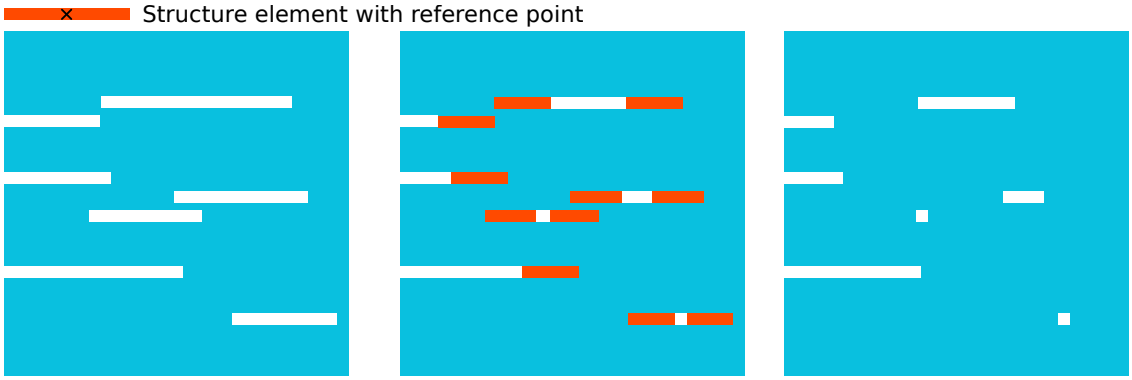


**Figure 3.11:** The erode operator. Left: input image provided by the dilate operator, white pixels are hit pixels. Center: after applying the erode operator, the pixels changed to not hit pixels are marked in red. Right: processed closed image, the gaps have been fixed and the length of the original lines restored (cf. left image in figure 3.10)

with pixels at the left and right boundaries will be excluded from further processing.

The application to the data taken at the experiment is shown in figure 3.12.

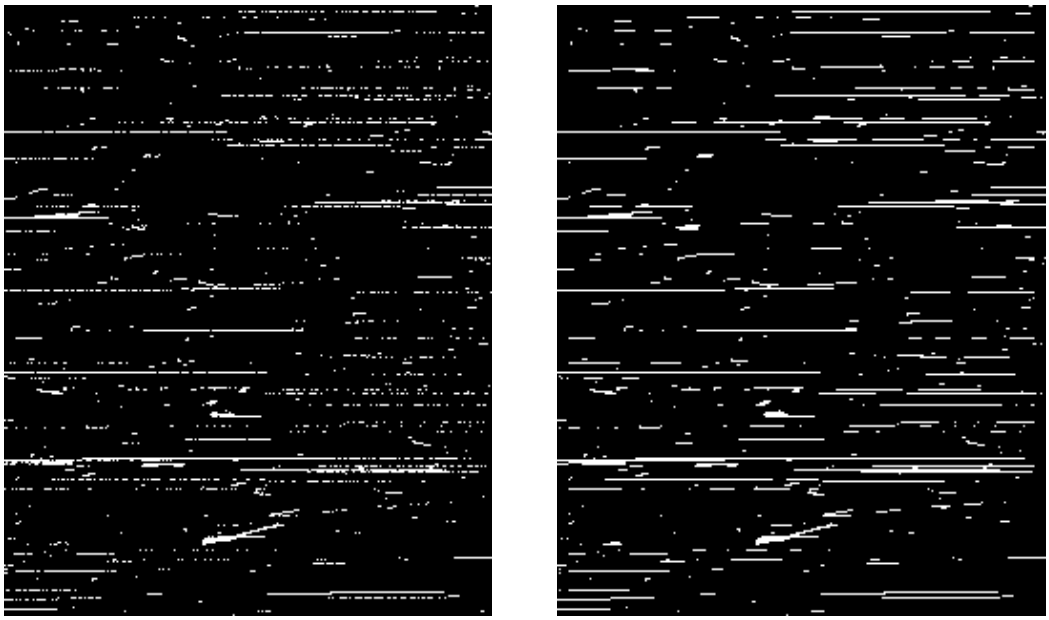

**(a)** Original data **(b)** Closed data

**Figure 3.12:** The application of the closing operator

### 3.4.3 Line detection algorithm

As mentioned earlier, the Hough transform has shown to be inappropriate for the line detection and reconstruction in the measured data. To improve the quality of the data, the closing operator was applied as described in the last section. The Hough transform was applied once again to the fixed lines, but the described problems persisted. Therefore, a special code has been developed that takes into account the special features of the data set.

Because of geometrical reasons, the lines have no or only a very shallow slope, as illustrated in the sketch in figure 3.13. With a lateral beam widening of about $\pm 1\ \mathrm{cm}$ at Bragg peak depth and using that the detector was set up such that its mid-point had the same height as the beam axis, the maximum height change for a track over the whole width of the detector can be calculated as

$$|\Delta\, y_{max}| = 6.8\,\mathrm{cm}\,\left(1 - \frac{d}{d + 1.28\,\mathrm{cm}}\right).$$

With a row height of $425\,\mu\mathrm{m}$, the maximal number of different rows that can be transversed by a pion is therefore three for the $d = 1.4\,\mathrm{m}$ distance used in the experiment.

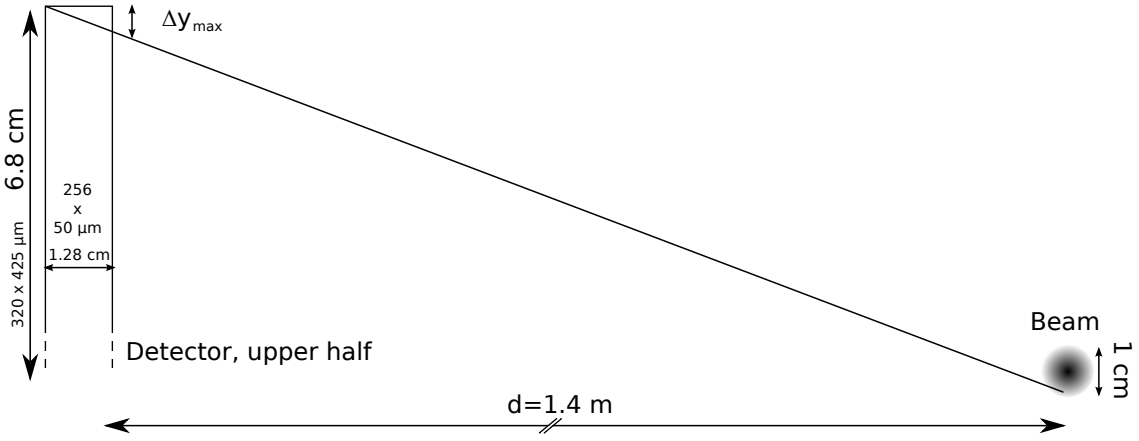


**Figure 3.13:** Sketch of the determination of the maximum height change of a track

This fact formed the basic idea of how a self-made line detection algorithm can be defined and optimized in detecting nearly horizontal lines.

The algorithm was written in C and was split into sub-functions for the different tasks. A flow chart of the functions is depicted in figure 3.14.

### Loading

The first function loads the raw data file and stores it into a $320 \times 256$ binary array as each pixel only contains the information if it was hit or not. Therefore, the size of the data set to process is very small ($320 \times 256\,\mathrm{bit} = 10\,\mathrm{kByte}$) and the time needed for the processing is accordingly short.

### Dilating and eroding

The loaded array is handed over to the closing function that consists of the dilate and the erode function. The dilate function has a 15 pixels long horizontal line as structure element which is moved over the array pixel by pixel. The procedure is the same as described in section 3.4.2: Each time, the pixel lying under the midpoint of the structure line is regarded. If one of the pixels under the structure element has been hit, the midpoint pixel is switched on. As this affects the outcome of further evaluations, i.e. of the neighboring pixels, the results of the dilate function are stored into another array of the same size.

The erode function has the same 15 pixels long structure line and works as described above. Again, the results of the erode function are stored into a new array to avoid effects of already eroded parts of the image to non-eroded parts.

### Line detection

The line detection function consists of three parts. The first part scans through the array created by the closing function. If a hit pixel is found, its position is saved as one endpoint of the line and handed over to the part that investigates its adjacent neighbors. As most lines are horizontal, it is checked if the right neighbors have also been hit. If the last hit pixel is reached, the third part is called which checks if the adjacent pixels in the row above or beneath have been hit. If this is the case, three slopes of the lines that could fit into the detected track are calculated: the minimal, the average and the maximum slope.

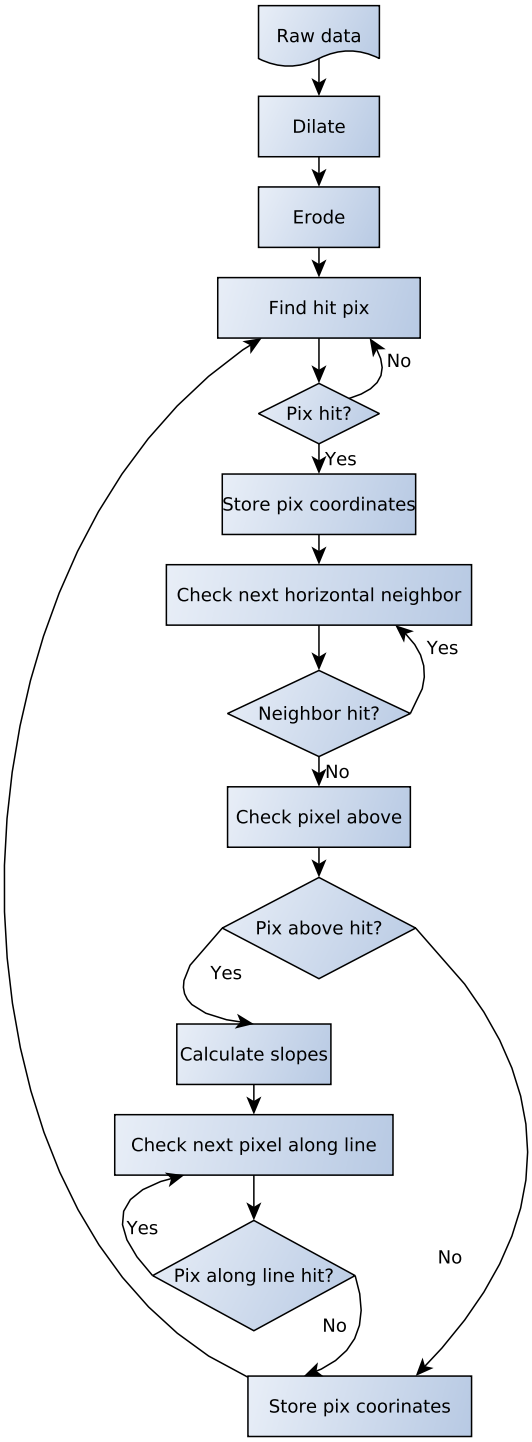


**Figure 3.14:** Flow chart of the line detection algorithm

For all three slopes, the position of the next expected hit pixel is calculated and evaluated. If no further hit pixel is found, the last found hit pixel is regarded as the other endpoint of the line. The longest of the three lines with the different slopes is taken and all pixels marked such that they can not be endpoints of another line. Finally, the endpoints of the line are returned for the further analysis.

### Annihilation vertex distribution reconstruction

The next step is to transform the detected lines into an annihilation vertex distribution along the beam axis. Therefore, a ROOT script was created that transforms the endpoints of the lines into the laboratory coordinate system, whose origin was chosen to be the entrance window of the water phantom, with the z axis along the beam axis. This includes a rotation and a translation.

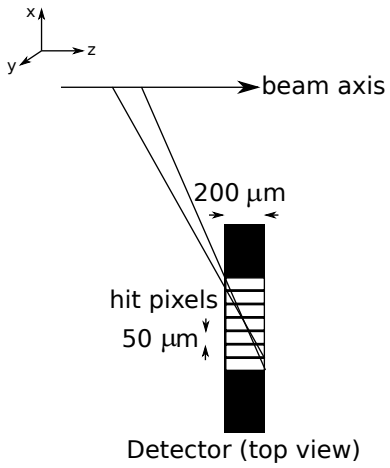


**Figure 3.15:** Sketch of the determination of the annihilation vertex distribution

The idea behind the annihilation vertex distribution reconstruction is to regard a track in the detector as volume. Assuming that the pions only entered the detector from the left side, which is fullfilled for the larger angles of the detector, the $50\,\mu\mathrm{m} \times 425\,\mu\mathrm{m}$ side of the first hit pixel can be seen as entrance window. The same assumption is used for the right side of the last hit pixel, which forms the exit window. By this, the area of origin at the beam axis of the pion along x and z can be reconstructed as can be seen in figure 3.15. In principle, this method allows a two-dimensional reconstruction of the annihilation vertex distribution at the beam axis plane, but the vertical resolution is only about $5\,\mathrm{cm}$ for full track lengths and decreases for shorter tracks, because of the large vertical size of the pixels.

# 4 Results

For the analysis of the results, the methods described in chapter 3 are applied to the data taken in the run in September 2009.

## 4.1 First overview

In the first run, the detector was rotated to different angles to determine the overall behaviour of the track lengths. Clearly, for each angle, the pions created at the position where the edge of the detector is pointing at, leave the longest tracks behind as they travel through the whole detector. For larger distances from that position, the tracks become shorter and shorter, depending on the angle between the pion direction of flight and the detector. The relative amount of tracks with a certain length for a given angle provides a measure of the relative intensities of pions along the beam axis. An overview is given in the histograms in figures 4.1–4.4. Here, the track length distributions for three different detector angles are shown (the angle scale provided at the detector mounting had an arbitrary, but fixed offset). In figure 4.1, the detector was pointing with its edge towards the beam exit window of the beam pipe. As there are no full length tracks, almost no antiprotons annihilate in this region. The maximum at track lengths of about 30 pixels is due to the Bragg peak at deeper depths, because most antiprotons annihilate there and thus, the amount of pions coming from that region is high. The detector was pointing towards the Bragg peak in figure 4.2, where the relative amount of the longest tracks is highest. In figure 4.3, the detector was pointing to a region few centimeters distal to the Bragg peak. By that, the pions can only penetrate through the detector from one side, which avoids ambiguities in the reconstruction. Therefore, this angle will be used for further analysis. In figure 4.4, the detector pointed to a region far away from the distal

edge of the Bragg peak. Again, the tracks are shorter and the Bragg peak corresponds to track lengths of about 20 pixels.

To transform the information of the histograms into an annihilation vertex distribution along the beam axis, the number of the longest tracks ($240 - 260$ pixels) are normalized to the amount of tracks that correspond to the first few centimeters (the so-called plateau region) in the entrance channel. As most pions come from the Bragg peak region, the maximum of the histogram in figure 4.5 is regarded as the Bragg peak. This is where the origin of the z axis has been put, the distances have been transformed from the detector angle and the known distance of the detector to the beam axis.

Figure 4.5 is, however, only a rough overview of the vertex distribution for two reasons. On the one hand, the normalization is not unique, as for medium angles, the pions can penetrate through the detector from both sides, i.e. from different positions, but still leaving tracks of the same length behind. On the other hand, the resolution is for geometrical reasons only about $5\,\mathrm{cm}$ when only taking into account the longest tracks that cross the whole detector (cf. figure 5.1).

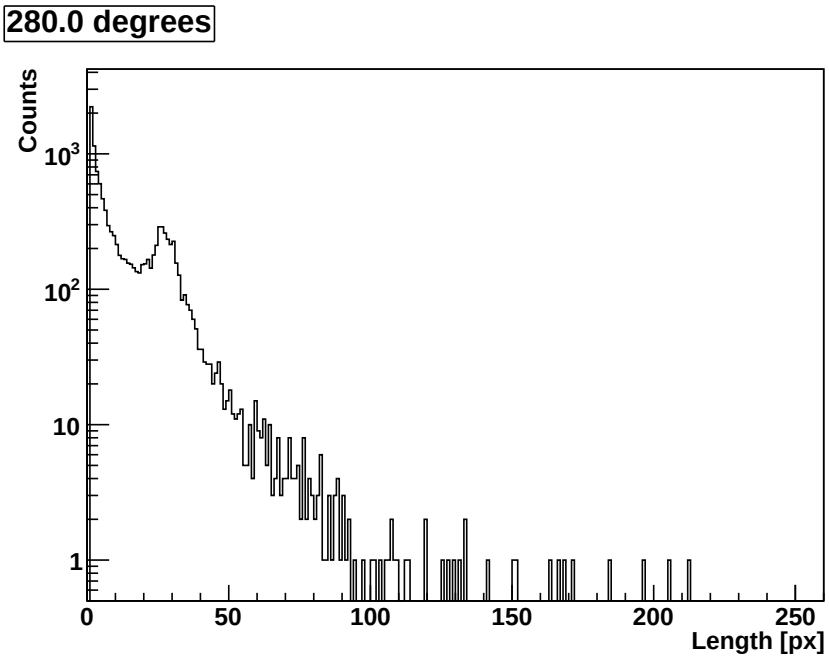


**Figure 4.1:** Track length histogram at a detector angle of $280$ degrees, $8.5$ degrees proximal to the Bragg peak

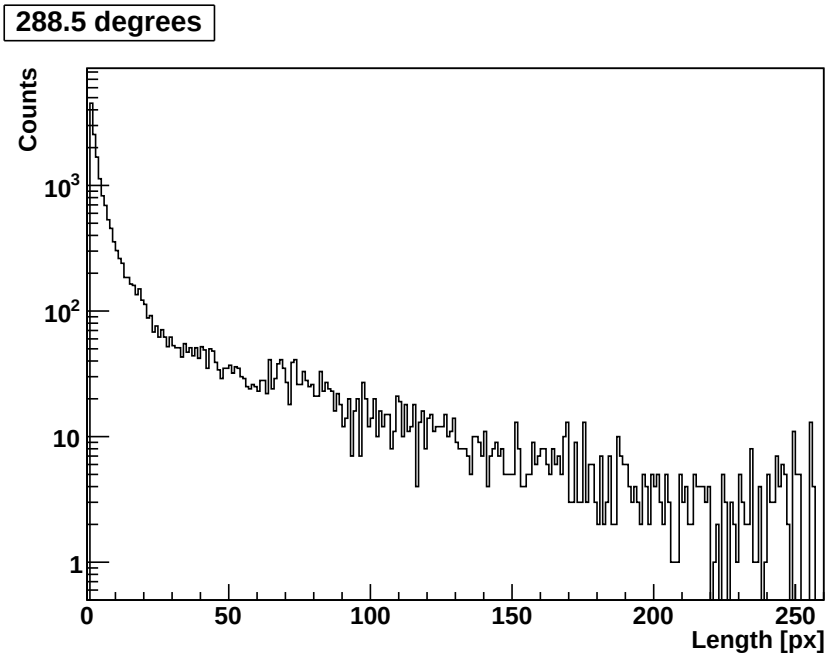


**Figure 4.2:** Track length histogram at a detector angle of $288.5$ degrees. This angle is estimated to point to the Bragg peak

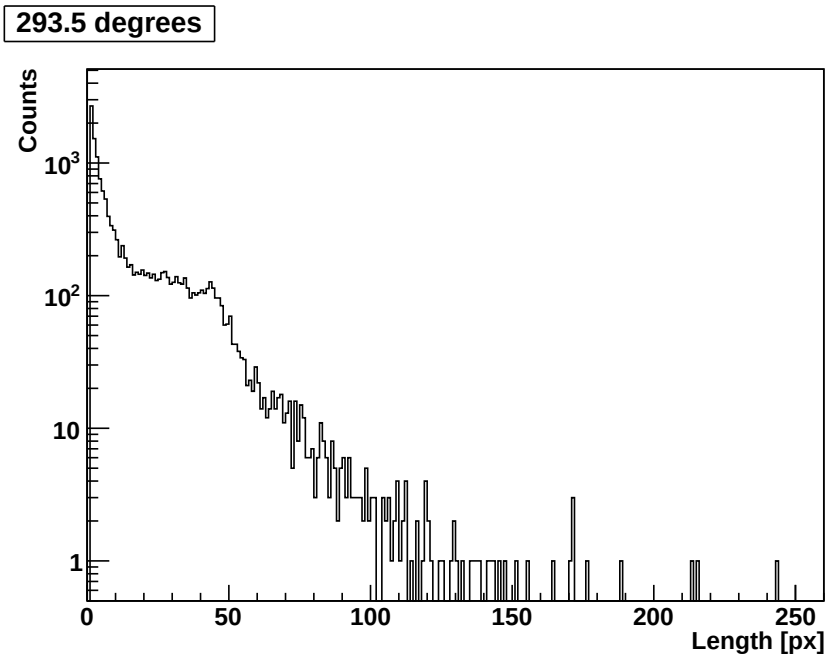


**Figure 4.3:** Track length histogram at a detector angle of $293.5$ degrees, $5$ degrees distal to the Bragg peak

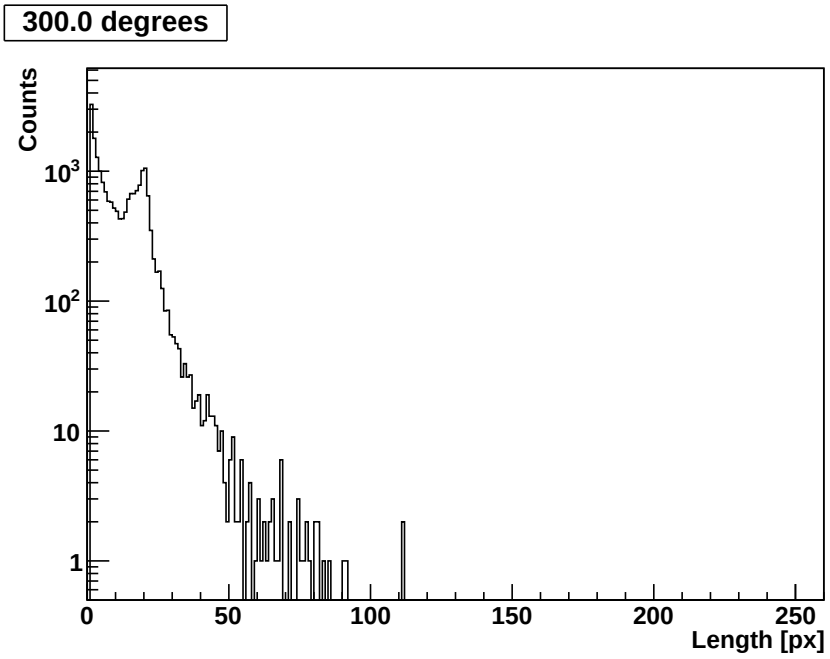


**Figure 4.4:** Track length histogram at a detector angle of $300$ degrees, $11.5$ degrees distal to the Bragg peak

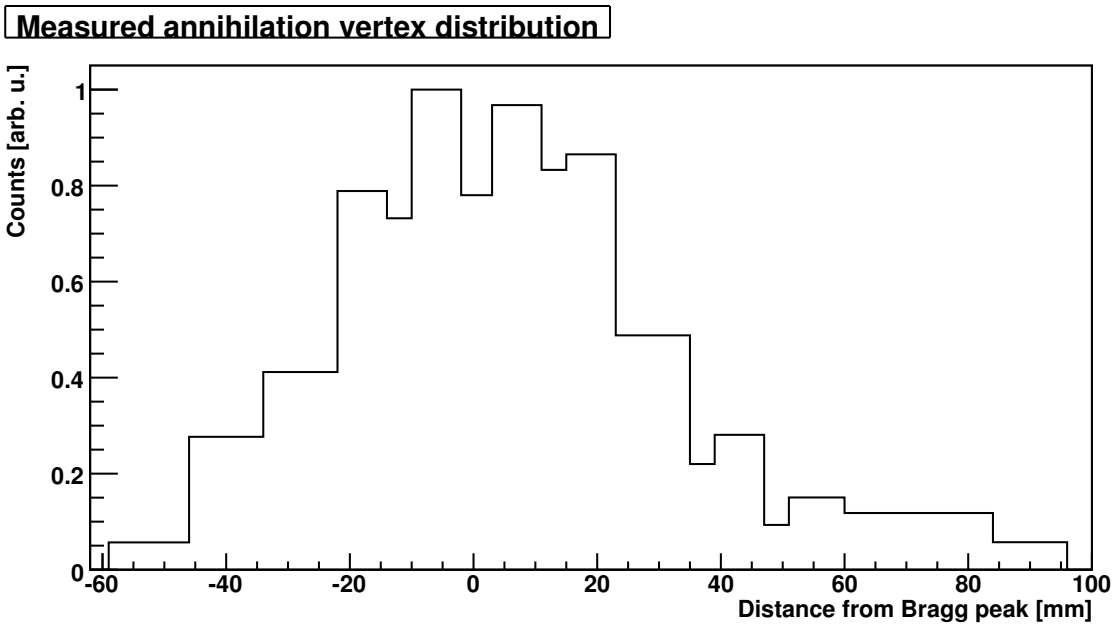


**Figure 4.5:** Relative intensities of the longest tracks for each detector angle. The angles have been converted to lengths along the beam axis. The detector angle corresponding to the origin is $288.5$ degrees

## 4.2 A deeper look

As mentioned above, only sufficiently large detector angles are used to ensure an unambiguous annihilation vertex distribution. The detector angles greater than $292.5°$ have been chosen as the track length distribution still reaches longer track lengths so that the whole spectrum of lengths can be used for the vertex reconstruction. The data set contains tracks created by about 100 spills of antiprotons for each angle taken in the run in September 2009.

As described in chapter 3, the endpoints of the lines detected by the self-written C-code are handed over to a ROOT script that does the calculation of the vertex distribution. The bin size was chosen to be $1\,\mathrm{mm}$. As the relative position of the detector along the beam axis (z axis) with respect to the water phantom has not been measured, the depth axis was offset such that the Bragg peak is located at about $10\,\mathrm{cm}$, which has been measured directly by another experiment. The results are shown in figures 4.6–4.9.

As all measurements were done in parasitical mode, i.e. they were carried out independently of the other experiments. Thus, the set-up in the beam axis was frequently changed. For all the data, cell samples were irradiated, but the samples exchanged and the number of degraders changed to produce a spread-out Bragg peak. Each degrader shifts the Bragg peak $2.38\,\mathrm{mm}$ proximal. However, the effect of degraders can not be clearly seen in the figures. One reason is that the data were taken not parallel to the production of such a spread-out Bragg peak, such that the weights of the different single Bragg peaks are wrong.

The maximum in the figures denotes the Bragg peak region. The larger the angle is, the shorter the track lengths representing that region are. In figure 4.6, i.e. only 4 degrees behind the angle pointing directly towards the Bragg peak, the resolution is therefore best, whereas the resolution in figure 4.9 is worst. Here, the change of track lengths by one pixel corresponds to a change of position of about $1.5\,\mathrm{cm}$. Towards deeper depths, the resolution becomes better for geometrical reasons. There the track lengths are longer and the projection to the beam axis narrower.

In all figures, long tails behind the Bragg peak can be observed, meaning that pions appear to have been created in significantly deeper depths. As this can not be the case for physical reasons, because all of the antiprotons stop in the Bragg peak region with an insignificant

range straggling, further investigation has been done on this issue. It has turned out that the elastic scattering of the pions between the Bragg peak and the detector has a large impact on the resolution, as is further discussed in section 5.1.

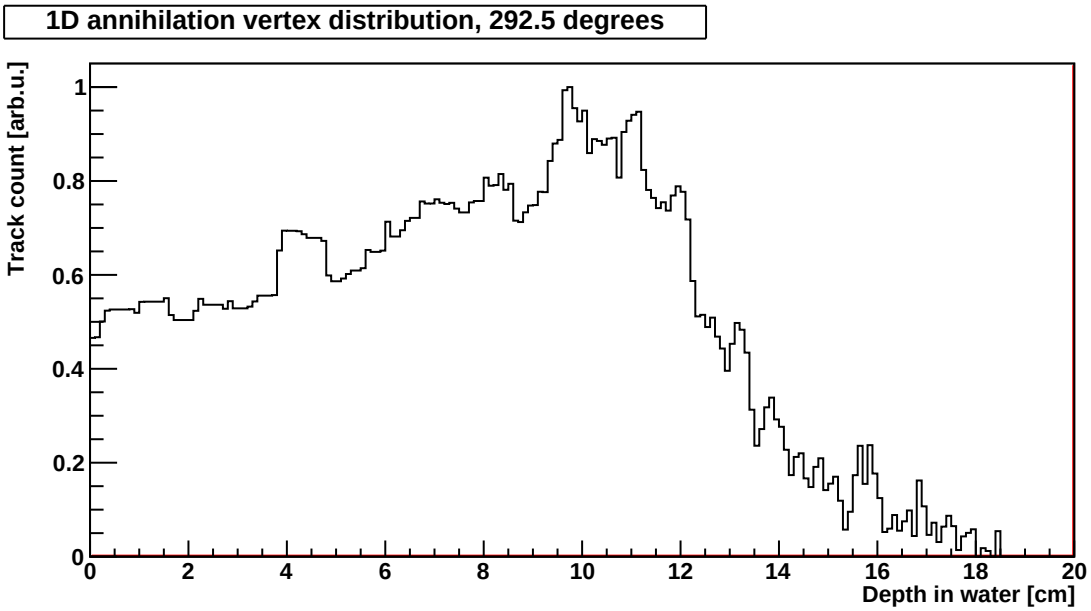


**Figure 4.6:** Reconstructed 1-dimensional annihilation vertex distribution for the detector angle of 292.5 degrees, 4 degrees distal to the Bragg peak

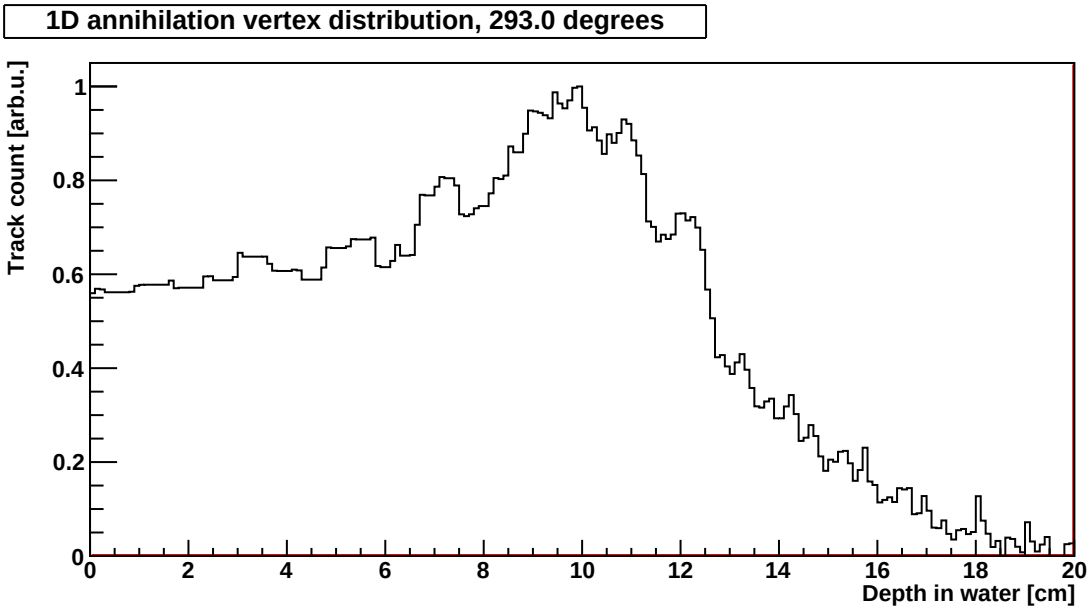


**Figure 4.7:** Reconstructed 1-dimensional annihilation vertex distribution for the detector angle of 293.0 degrees, 4.5 degrees distal to the Bragg peak

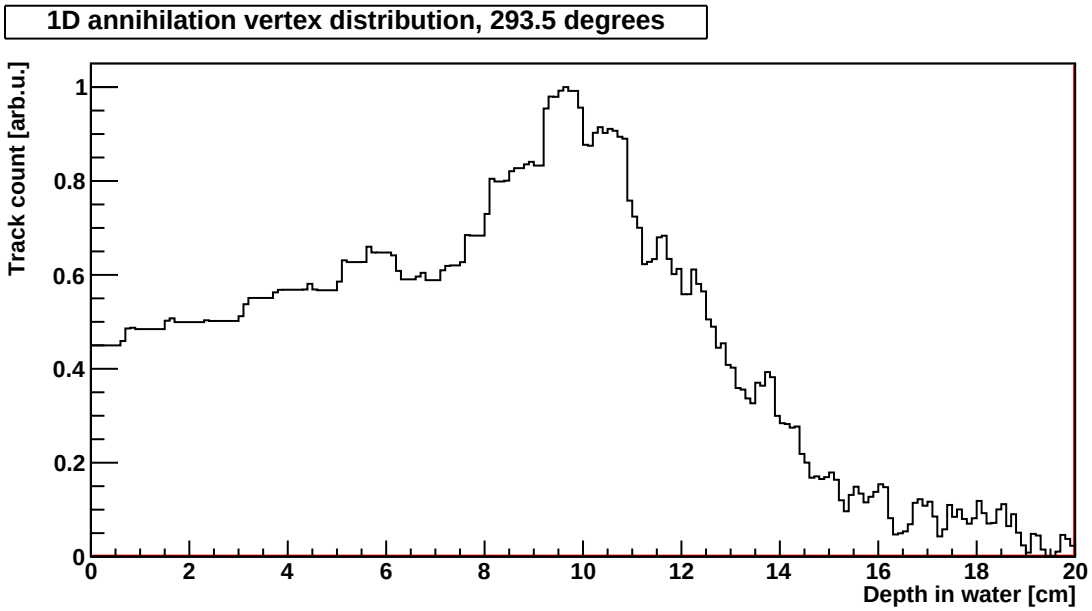


**Figure 4.8:** Reconstructed 1-dimensional annihilation vertex distribution for the detector angle of 293.5 degrees, 5 degrees distal to the Bragg peak

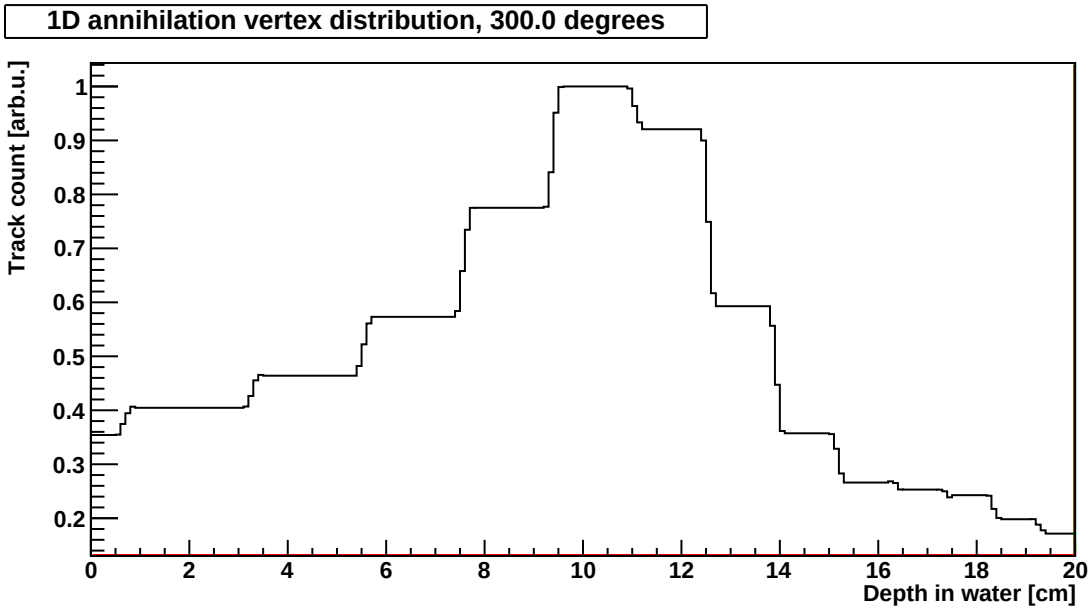


**Figure 4.9:** Reconstructed 1-dimensional annihilation vertex distribution for the detector angle of 300.0 degrees, 11.5 degrees distal to the Bragg peak

# 5 Discussion

## 5.1 Experimental resolution

The experimental resolution depends on two factors:

- Detector resolution, determined by detector parameters and the physical set-up
- Resolution limited by scattering

### Detector resolution

The cuboid pixel dimensions ($50\,\mu\mathrm{m} \times 425\,\mu\mathrm{m} \times 200\,\mu\mathrm{m}$) make the experimental resolution depend on how the detector is positioned. In the experimental set-up, it was placed with its $200\,\mu\mathrm{m}$ edge parallel to the beam axis, and the $425\,\mu\mathrm{m}$ edge in vertical direction. Thus, the pions propagate through the detector along the $256$ pixels with $50\,\mu\mathrm{m}$ length. As they enter the detector from only one side, the effective resolution is determined by the projection of the $50\,\mu\mathrm{m} \times 425\,\mu\mathrm{m}$ area on the plane perpendicular to the beam axis, which depends on the detector angle and on the angle between the direction of flight and the detector. The resolution becomes better for long tracks and deterioates towards short track lengths as the projection of the track to the beam axis plane becomes larger and larger, as shown in figures 5.1 and 5.2. For a track reaching from one end of the detector to the other, the resolution decreases to only $4\,\mathrm{cm}$ for geometrical reasons (bottom picture in figure 5.1). However, lines of such length are not expected because the detector was either rotated or moved along the beam axis such that no particles are created at the positions corresponding to these lengths.

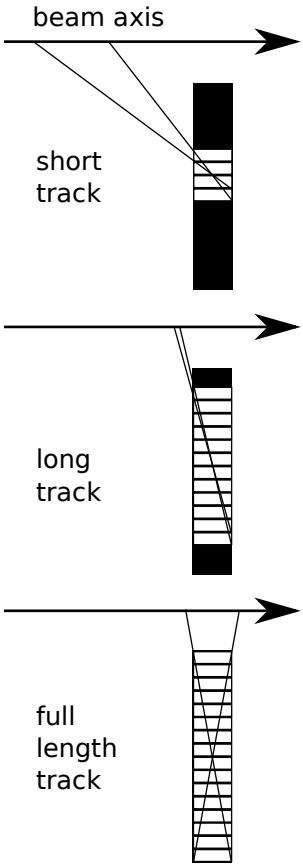


**Figure 5.1:** The detector resolution depends on the track lengths

The method described in section 3.4.3 basically allows a 2-dimensional annihilation vertex distribution reconstruction. The large height of the pixels, however, limits the vertical resolution only to $5\,\mathrm{cm}$ or worse.

Before the reconstruction method described earlier had been developed, the idea was to relate the amount of full-length tracks to the number of tracks corresponding to the entrance region or all measured tracks to have a measure for the vertex distribution. This would have had the drawback that by using the full-length tracks, the resolution would have been restricted to $4\,\mathrm{cm}$. An approach to overcome this would be to turn the detector such that its long edge points to the beam axis (figure 5.3), which would have improved the resolution to about $4\,\mathrm{mm}$. Simulations showed, however, that in this case too much silicon is in the pions' path, making them scatter in the detector volume (figure 5.4).

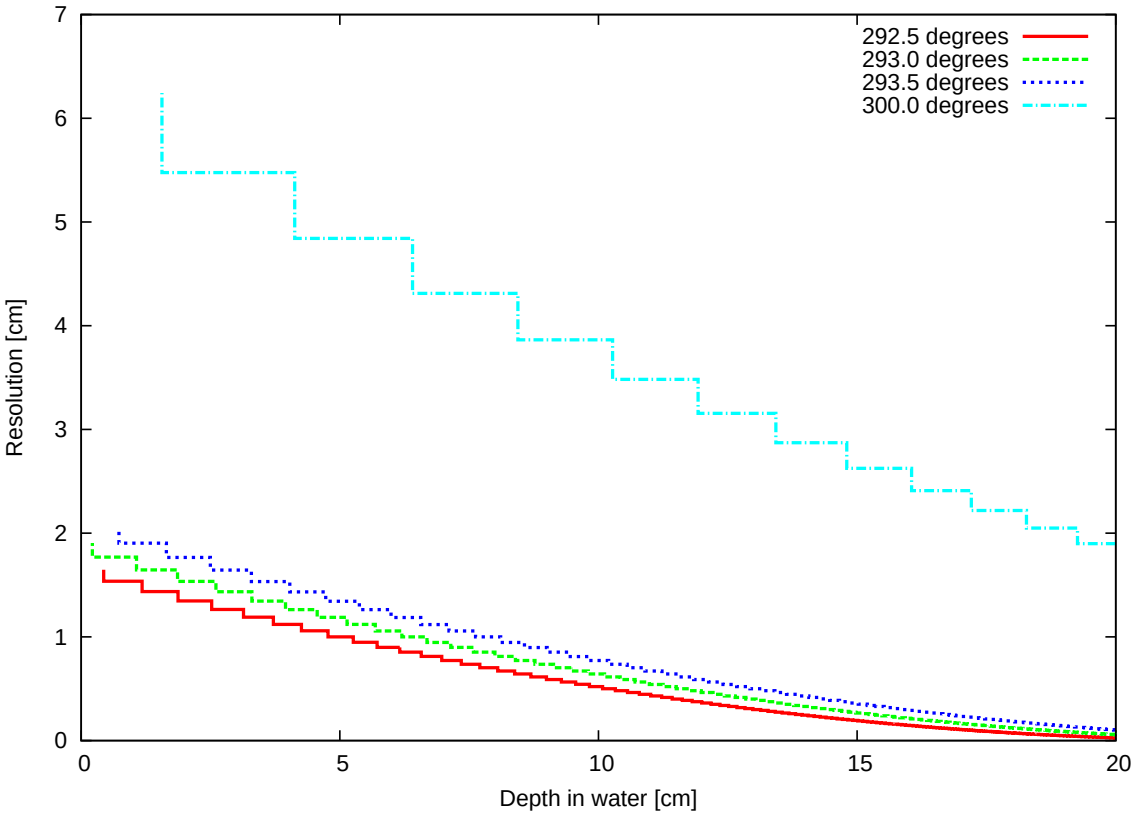


**Figure 5.2:** Detector resolution for the different angles.

As this would eliminate the possibility to detect straight tracks needed for the calculation of the vertex distribution, the proposed set-up for the second run was discarded. Furthermore, the problem has been overcome with the reconstruction method described in section 3.4.3.

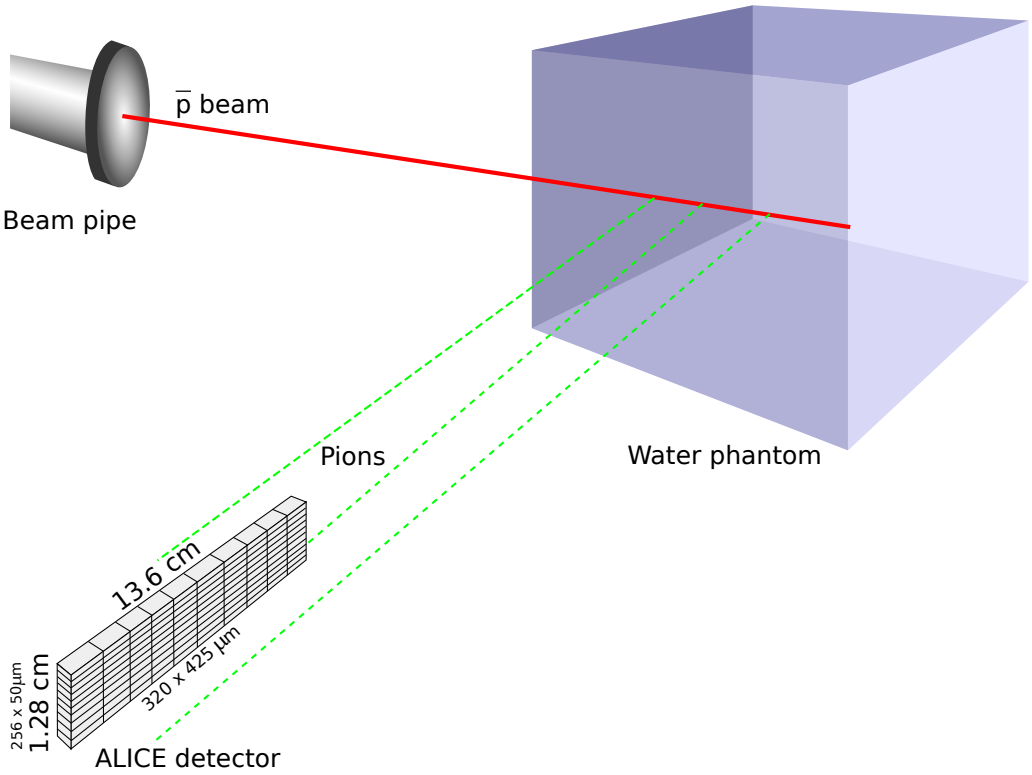


**Figure 5.3:** Discarded set-up

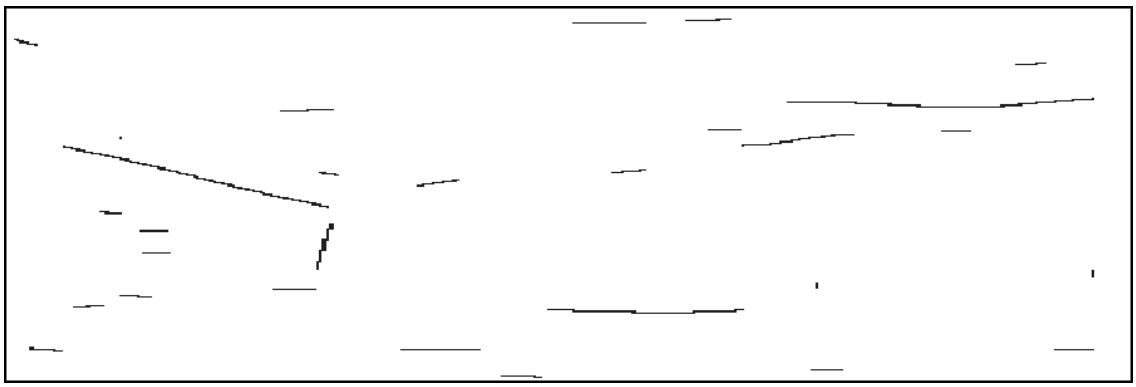

**Figure 5.4:** Tracks bent by scattering in the silicon detector as expected from simulations for the proposed alternative set-up

### 5.1.1 Pion scattering

All charged particles scatter off the surrounding matter.

The scattering angles for Coulomb scattering can be calculated with Rutherford's cross section:

$$\frac{d\sigma}{d\Theta} \propto \frac{Z_1^2 Z_2^2}{E^2} \cdot \frac{1}{\sin^4 \frac{\Theta}{2}}$$

with $Z_1$, $Z_2$ the charge of the scattering particles, $E$ the energy of the incident particle, and $\Theta$ the scattering angle. The angle $\Theta_{1/e}$, where the angular distribution has fallen to 1/e, for multiple Coulomb scattering can be approximated for small scattering angles and low energy loss by Highland's formula [Hig75], [Lyn91]:

$$\Theta_{1/e} = S \frac{\sqrt{X/X_0}}{p\beta c} \left[1 + \varepsilon \log_{10}(X/X_0)\right],$$

with $S = 14.1\,\mathrm{MeV}$, $X$ the thickness of the absorber, $X_0$ the radiation length, $p$ the particle momentum, $\beta$ the particle velocity in terms of the speed of light, and $\varepsilon = 1/9$ a correction factor.

A rough estimation using the above formula and radiation lengths found in [Amson] shows that the pions do not scatter significantly in the $1.4\,\mathrm{m}$ air between the water phantom and the detector, but in the water itself. There, the $\Theta_{1/e}$ scattering angle is about $0.05\,\mathrm{rad}$, which results in a rms spread of $7.5\,\mathrm{cm}$ in $1.4\,\mathrm{m}$ distance or a FWHM of $11\,\mathrm{cm}$. This is a severe degradation of the achievable resolution. The spread has also been shown in simulations, where a monoenergetic, non-divergent beam of charged pions of the typical energy provided upon antiproton annihilation was shot from inside the water phantom to a virtual detector plane, measuring the broadened beam (cf. figure 5.5).

However, there is no possibility to overcome this drawback, as the detector cannot cope with the high particle densities in smaller distances. The internal buffer would overflow as described in section 3.2.

For typical clinical beam parameters, the particle intensities are much lower than the instantaneous very high intensities provided in the antiproton pulses at the Antiproton

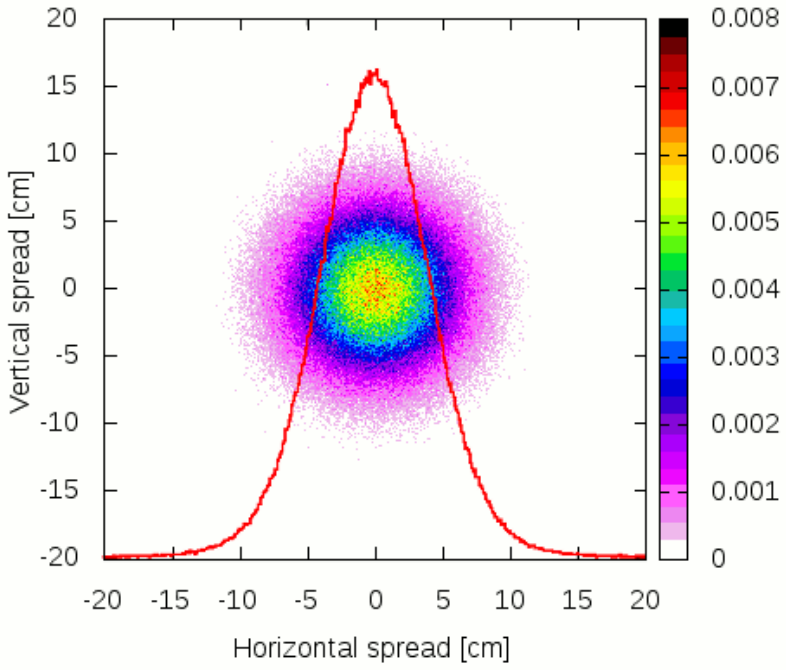


**Figure 5.5:** Pion beam broadening due to multiple Coulomb scattering on the way to the detector. The FWHM obtained by a fitted Gaussian is about $9\,\mathrm{cm}$

Decelerator ($10^6 - 10^8\ \mathrm{s}^{-1}$ typical, compared to $10^{13}\ \mathrm{s}^{-1}$ at the AD). Therefore, there is no strong need to find solutions to this problem as it would not exist in realistic medical applications. A theoretical scenario with the detector placed in only $30\,\mathrm{cm}$ distance to the water phantom is described in section 5.2.2.

## 5.2 Comparison with Monte-Carlo simulations

Parallel to the experiment, simulations using the Monte-Carlo transport code FLUKA [Bat07] [Fas05] have been carried out. It is a closed-source code written in FORTRAN77 and has been successfully applied to model various aspects in the ACE experiment, like the depth dose curve of antiprotons in water [Bas08a], the response of alanine detectors to antiproton irradiation [Bas08c], as well as to achieve absolute and relative dosimetry [Bas08b], the LET spectrum [Bas09], and real-time imaging [Kan10].

All the simulation parameters like geometry, scoring of energy, particles etc. are implemented by creating an input file which is read by the FLUKA code.

To simulate the imaging in the ACE experiment, the water phantom including the thin beam entrance window, the water, the air between phantom and the detector and the detector have been modeled in terms of size and material composition.

The detector has only been modeled as a pixelized silicon slab with the dimensions of the real detector that was used. The basic FLUKA modeling features limit the implementation of the various angles to the simplest configuration, i.e. the detector standing perpendicular with its $1.28\,\mathrm{cm}$ edge with respect to the beam axis. To avoid track ambiguities, the whole detector was shifted $10\,\mathrm{cm}$ distal to the Bragg peak (cf. figure 5.6).

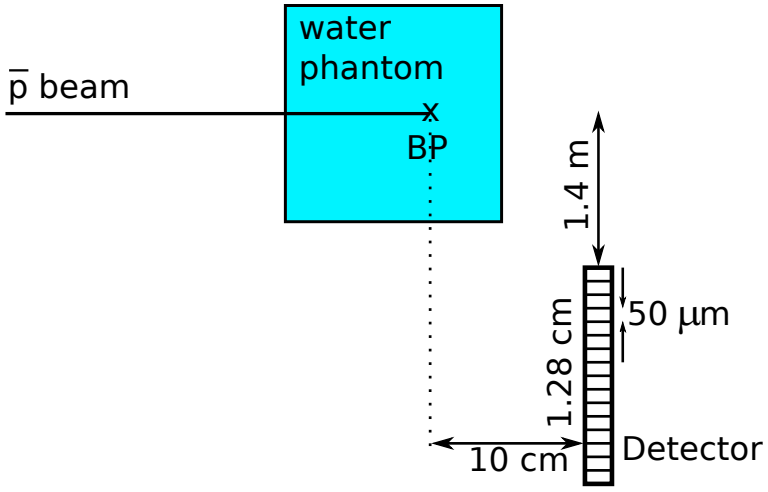


**Figure 5.6:** Top view of the set-up used in the simulation

FLUKA allows to separate the signal into the contributions of each particle species. Therefore, only the signal produced by pions has been scored, as well as the signal produced by all charged particles. For the whole simulation, no detector response model has been used, but only the presence of particles has been measured, which is of course a strong simplification.

50 pulses of $4 \cdot 10^7$ antiprotons have been simulated to obtain sufficient statistics.

The result is shown in figures 5.7 and 5.8. Except of the higher underground signal, the obtained annihilation vertex distributions do not differ much between pions only and all

charged particles. Compared to the distributions obtained from the experiment (figures 4.6–4.9), however, there are significant deviations:

- The position of the Bragg peak differs by about $1\,\mathrm{cm}$. This is however likely due to the fact that the position of the detector with respect to the water phantom, especially its position along the beam axis, has not been measured precisely, which could result in a deviation of a few centimeters.
- The width of the reconstructed Bragg peak from the experiment is larger than the width obtained from the simulation. Possible reasons are the use of degraders in the experiment which shift the Bragg peak by a few millimeters along the beam axis and have not been considered in the simulation, and imprecision of the line detection algorithm. The latter could either be the imperfectness of the algorithm such that it does not detect the full length of a track, or the imperfectness of the track itself: the algorithm only detects lines that are bounded by two hit pixels. But if the track continues without a response of the adjacent pixels, the true length of the line can not be determined, which introduces an additional error.

Furthermore, the experimental set-up differs from the set-up used in the simulation, as the implementation of rotated detector and pixel geometries is limited in the basic FLUKA features.

### 5.2.1 Scattering kernels

An idea to overcome the limitations by pion scattering is to use Monte-Carlo simulations to build a scattering kernel database for defined pion origins. Therefore, antiprotons with no residual kinetic energy were artificially released at defined depths along the beam axis in the water phantom and the signal produced by the emerging pions measured and stored in a database. The signal produced by antiproton irradiation can then be decomposed and fitted to the contributions measured for the database. However, it is a large effort to build the scattering kernel set. For a desired resolution of $5\,\mathrm{mm}$, about 30 different positions of defined antiproton annihilations along the beam axis have to be simulated, each with sufficient statistics. Each of the positions would need about two days of computing time of the whole computing cluster provided by the DKFZ (German Cancer Research Center)

group. As the actual problem does not appear for a clinical environment (cf. section 5.1.1), the scattering kernel method was therefore abandoned.

### 5.2.2 A more clinical example

The distance of the detector to the water phantom has been decreased in another simulation to $30\,\mathrm{cm}$ from the outer wall of the water phantom to resemble a more clinical situation. The angle $\Theta_{1/e}$ is still the same as in section 5.1.1, but because of the smaller distance this only corresponds to a rms spread of about $5\,\mathrm{mm}$ or a FWHM of about $4\,\mathrm{mm}$, respectively. The detector was therefore only shifted by $1\,\mathrm{cm}$ distal to the Bragg peak. Again, 50 pulses of $4 \cdot 10^7$ antiprotons have been simulated. The annihilation vertex reconstruction using all charged particles is shown in figure 5.9. Its maximum at $11.3 - 11.7\,\mathrm{cm}$ coincides perfectly with the shoulder in figure 5.10 and the peak in the differential antiproton fluence. The high signal in the entrance channel is due to the track detection algorithm which has problems in detecting tracks with slopes that extend over several pixel rows, such that a long track with slope is likely to be detected wrongly as many short tracks instead, which in turn are transformed into a more proximal position. This issue can however be fixed if necessary and is work in progress.

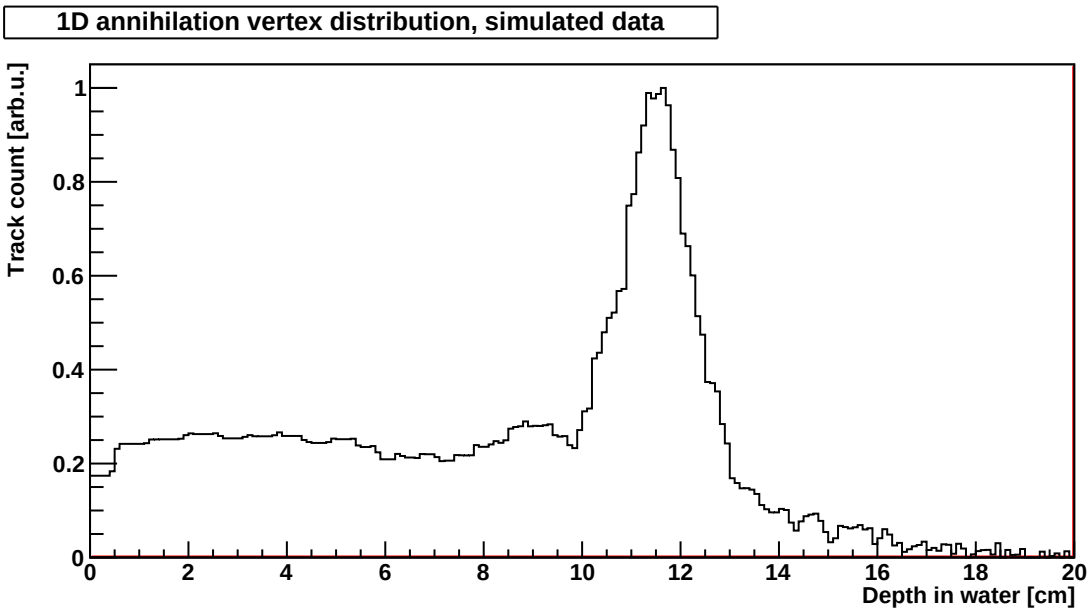


**Figure 5.7:** Reconstructed annihilation vertex distribution from simulation using pions only

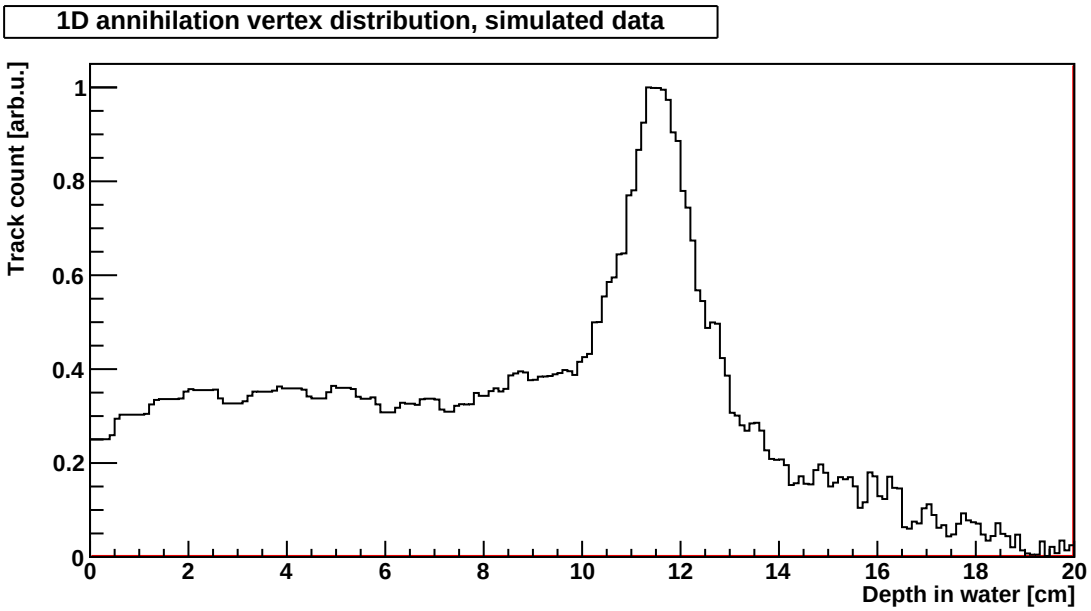


**Figure 5.8:** Reconstructed annihilation vertex distribution from simulation using all charged particles

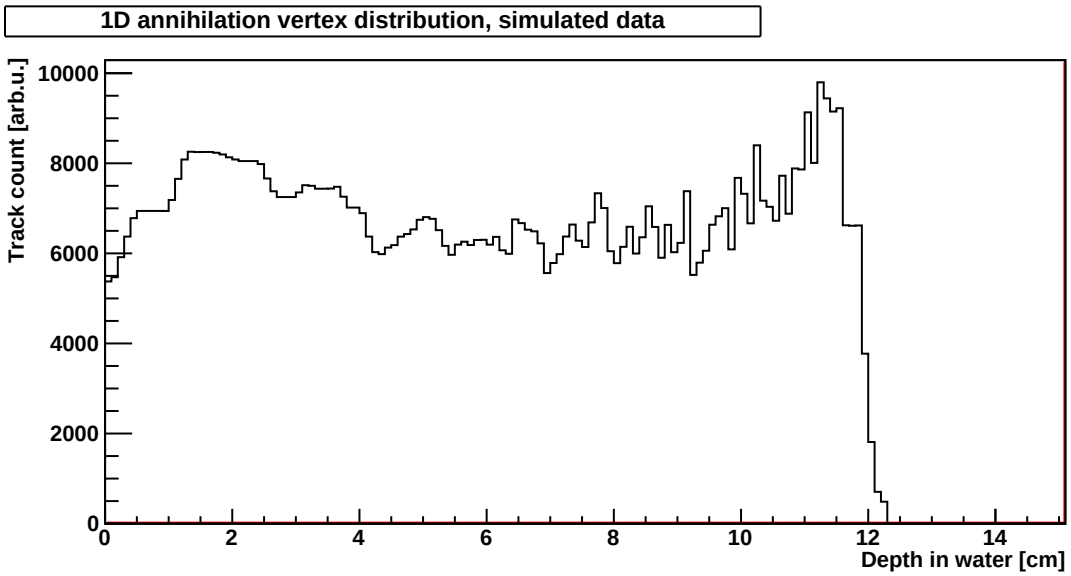


**Figure 5.9:** Reconstructed annihilation vertex distribution for the clinical example. The steep decrease at the distal end allows a precise determination of the range of the incident antiprotons.

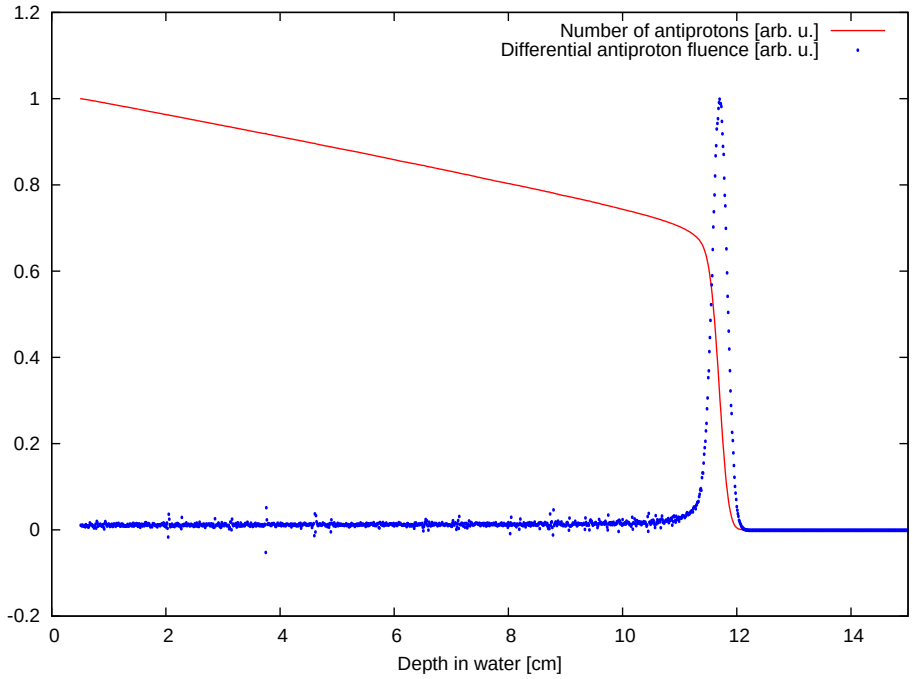


**Figure 5.10:** Number of antiprotons and the differential antiproton fluence plotted against the depth in water

## 5.3 Real-time?

The title of this thesis suggests that the annihilation vertex distribution can be obtained in real-time. This is basically true, but has not been shown directly in the experiment. The problem there is the pulsed nature of the antiproton beam provided by the Antiproton Decelerator (cf. section 2.5.1), where one pulse is extracted every $90$ seconds, and only a fraction of it is measured by the detector (cf. section 3.2). The track information obtained from such a pulse is therefore not sufficient to image the annihilation vertex distribution. However, one pulse of about $3 \cdot 10^7$ antiprotons corresponds to a dose of only about $30\,\mathrm{mGy}$ in the plateau region for the experimental setup (Gaussian beam shape, $\sigma = 4\,\mathrm{mm}$), and about $135\,\mathrm{mGy}$ in the Bragg peak, respectively [Bas08b]. Thus, about $7 \cdot 10^9$ antiprotons are needed for a typical dose per treatment fraction of $2\,\mathrm{Gy}$ in a $100\,\mathrm{ml}$ size tumor. In the simulation of the clinical example (section 5.2.2), already $3 \cdot 10^6$ antiprotons are sufficient (cf. figure 5.11) to have a range estimate of the antiproton beam. Therefore, range deviations in realistic clinical environments can be detected already during the very first part of the irradiation fraction. Together with a continuous antiproton beam in such environments and the fast data processing of the analysis algorithms, real-time imaging seems possible. In the experiment, however, the limitations due to saturation of the detector described in section 3.2 made shot-to-shot images of the annihilation vertex distribution impossible, even though the $3 \cdot 10^7$ antiprotons would be enough.

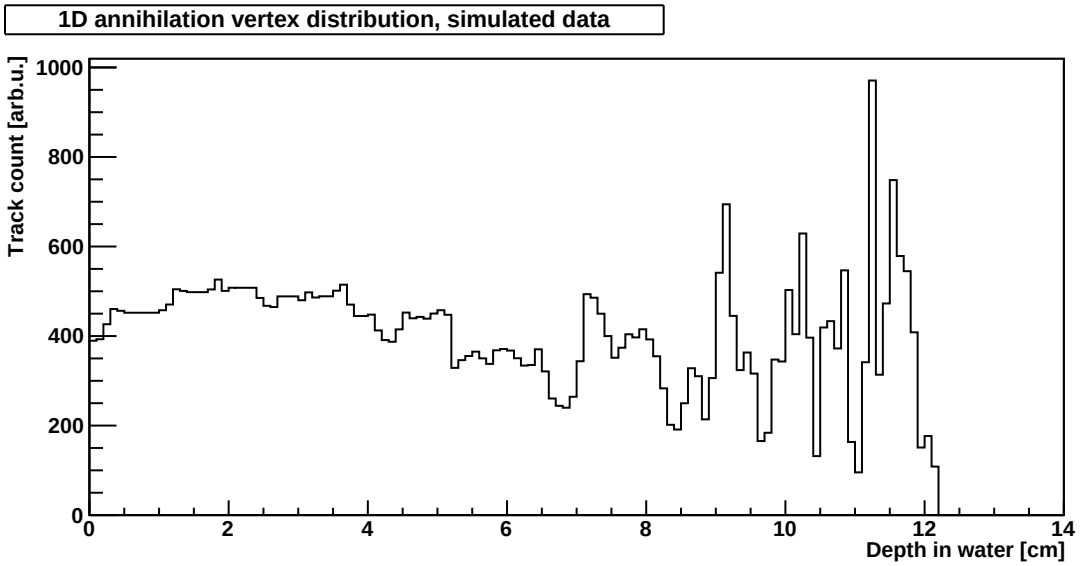


**Figure 5.11:** Reconstructed annihilation vertex distribution for the simulated clinical example. Only the first $3 \cdot 10^6$ antiprotons have been used

# 6 Conclusion, Outlook

This thesis showed that imaging of the stopping distributions during irradiation of a water phantom with antiprotons by tracking annihilation pions is feasible. In principle, this also holds for real-time imaging, which has however not been shown directly because of experimental limitations, as the antiprotons delivered by the Antiproton Decelerator come in bunches with long breaks in between. In simulations, however, it has been shown that the amount of incident antiprotons to obtain a reasonable signal is low compared to the amount which would be applied during one treatment fraction.

The method to reconstruct the annihilation vertex distribution is to use the track information obtained by a silicon pixel detector, which is traversed by pions created upon antiproton annihilation events.

The resolution in the experiment carried out is limited by two main factors:

- The pion scattering in the water phantom, which is magnified by the large distance between detector and water phantom.
- The gaps in the tracks measured by the detector. They introduce errors to the determination of the endpoints of the tracks. Furthermore, the gap fixing algorithm only works optimal for horizontal lines.

However, the limitations in this experiment would not exist for realistic clinical environments, as shown in simulations. There, it would be possible to use a more specialized detector with a sufficently high sensitivity, which can be placed closer to the patient because of the much lower beam intensity.

## 6.1 Open issues

### 6.1.1 Line detection

The self-made line detection algorithm only works well for completely horizontal lines. For lines, even with very shallow slopes, there are cases where the line has not been detected completely. A more elaborate algorithm that is capable to detect lines of any slope with high precision is desirable. Therefore, other image morphology concepts like pattern recognition or feature extraction techniques should be applied.

### 6.1.2 Detector response

To understand the detector response to the particles present in the experiment, more investigation has to be done to account for the gaps in the tracks observed in the measurements. Therefore, it is planned to use the Geant4 (another Monte-Carlo simulation code) Toolkit, where a thorough model of the detector has been developed by the ALICE SPD group, to simulate the ACE experiment once again and compare the data acquired in the experiment to simulated data.

In general, for dedicated clinical applications, detectors can be fabricated with a detection efficiency of one for every hit pixel sufficiently high above background such that much cleaner tracks can be obtained even without pattern recognition.

## 6.2 Outlook

### 6.2.1 Second run

In the second run carried out in June 2010, the idea was to determine the experimental resolution by artificially shifting the detector (or, from the detector's point of view, the Bragg peak) along the beam axis by $4\,\mathrm{cm}$ in steps of one centimeter to see if deviations of the antiproton range can be detected. By increasing the distance to the beam axis from $1.4\,\mathrm{m}$ to $1.8\,\mathrm{m}$, the vast majority of the tracks extend only over one pixel row, making the line detection more reliable. However, also the effect of pion scattering described in

section 5.1.1 becomes more pronounced. For an easier comparison with simulations, the detector has been set to an angle of $90°$ with respect to the beam axis.

A first reconstruction of measurements taken for two artificial shifts of the Bragg peak by $1\,\mathrm{cm}$ each is shown in figure 6.1. A shift can be seen, but is difficult to determine clearly. Further investigation is ongoing.

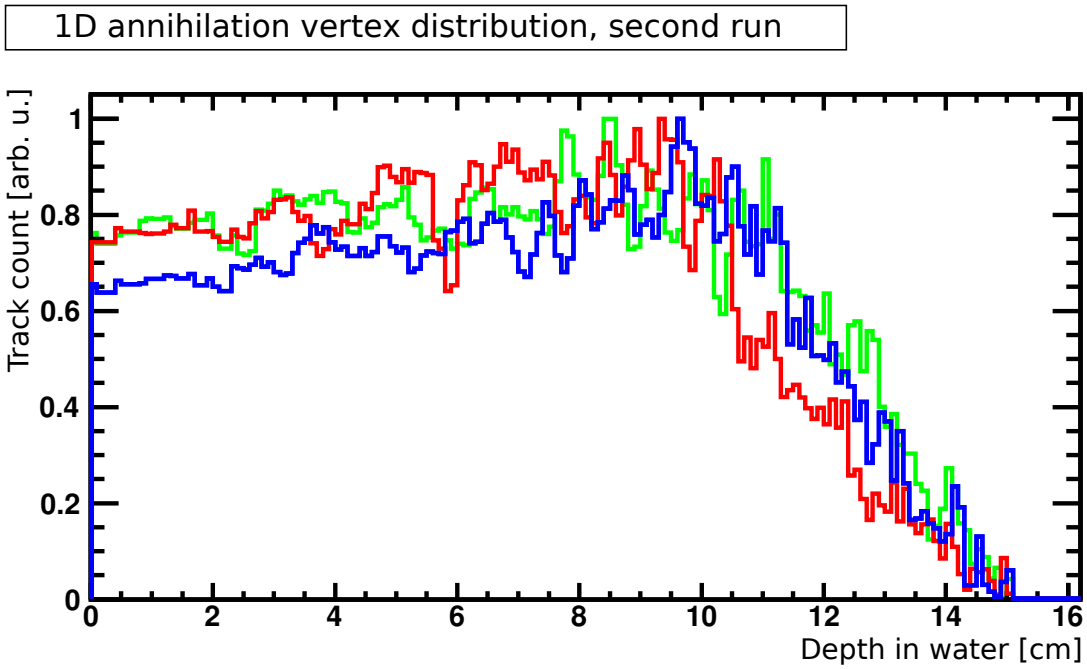


**Figure 6.1:** Annihilation vertex reconstructions for the second run. Black: unshifted distribution, green: the detector was shifted distal by $1\,\mathrm{cm}$. red: the detector was shifted proximal by another $1\,\mathrm{cm}$.

### 6.2.2 General

Further investigation will be done towards possibilities to measure the three-dimensional annihilation vertex distribution using a set-up with more detectors. The two-dimensional reconstruction is in principle already possible with the used set-up, but the vertical resolution is low because of the large pixel heights (cf. section 3.4.3).

Also, other detector set-ups with higher sensitivities could be used:

- Several ALICE SPD detectors stacked along the $200\,\mu\mathrm{m}$ edge, such that the pions travel through many detectors along their $200\,\mu\mathrm{m}$ side. Then the detector would be operated like in the ALICE experiment, and the traversing pions would generate a signal well above the threshold.
- A set of strip detectors. They combine a sufficiently high spacial resolution with a low amount of material which could interact with the pions.

This work will be continued in the framework of a PhD thesis.

# Bibliography


[Amson] AMSLER, C. and OTHERS (PARTICLE DATA GROUP): Review of Particle Physics. *Physics Letters* (2008 (and 2009 partial update for the 2010 edition)), vol. B667, URL http://pdg.lbl.gov

[Bai97] BAIRD, S A; BERLIN, D; BOILLOT, J; BOSSER, Jacques; BROUET, M; BUTTKUS, J; CASPERS, Friedhelm; CHOHAN, V; DEKKERS, Daniel; ERIKSSON, T; GAROBY, R; GIANNINI, R; GRÖBNER, Oswald; GRUBER, J; HÉMERY, J Y; KOZIOL, Heribert; MACCAFERRI, R; MAURY, S; METZGER, C; METZMACHER, K D; MÖHL, D; MULDER, H; PAOLUZZI, M; PEDERSEN, F; RIUNAUD, J P; SERRE, C; SIMON, Daniel Jean; TRANQUILLE, G; TUYN, Jan Willem Nicolaas and VAN DER SCHUEREN, A: The antiproton decelerator: AD (1997), (CERN-PS-97-036-HP):p. 3 p

[Bas08a] BASSLER, N; HOLZSCHEITER, M H; JÄKEL, O; KNUDSEN, H V; KOVACEVIC, S and THE AD-4/ACE COLLABORATION: The antiproton depth-dose curve in water. *Physics in Medicine and Biology* (2008), vol. 53(3):p. 793

[Bas08b] BASSLER, Niels; ALSNER, Jan; BEYER, Gerd; DEMARCO, John J.; DOSER, Michael; HAJDUKOVIC, Dragan; HARTLEY, Oliver; IWAMOTO, Keisuke S.; JÄKEL, Oliver; KNUDSEN, Helge V.; KOVACEVIC, Sandra; MØLLER, Søren Pape; OVERGAARD, Jens; PETERSEN, Jørgen B.; SOLBERG, Timothy D.; SØRENSEN, Brita S.; VRANJES, Sanja; WOUTERS, Bradly G. and HOLZSCHEITER, Michael H.: Antiproton radiotherapy. *Radiotherapy and Oncology* (2008), vol. 86(1):pp. 14–19

[Bas08c] BASSLER, Niels; HANSEN, Johnny W.; PALMANS, Hugo; HOLZSCHEITER, Michael H. and KOVACEVIC, Sandra: The antiproton depth-dose curve measured with alanine detectors. *Nuclear Instruments and Methods in Physics Research Section B: Beam Interactions with Materials and Atoms* (2008), vol. 266(6):pp. 929–936

[Bas09] BASSLER, Niels and HOLZSCHEITER, Michael: Calculated LET spectrum from

antiproton beams stopping in water. *Acta Oncologica* (2009), vol. 48(2):pp. 223–226

[Bas10] BASSLER, Niels; KANTEMIRIS, Ioannis; KARAISKOS, Pantelis; ENGELKE, Julia; HOLZSCHEITER, Michael H. and PETERSEN, Jørgen B.: Comparison of optimized single and multifield irradiation plans of antiproton, proton and carbon ion beams. *Radiotherapy and Oncology* (2010), vol. 95(1):pp. 87–93

[Bat07] BATTISTONI, G.; CERUTTI, F.; FASSO, A.; FERRARI, A.; MURARO, S.; RANFT, J.; ROESLER, S. and SALA, P. R.: The FLUKA code: description and benchmarking, vol. 896, AIP, pp. 31–49

[Ber98] BERGER, M. J. ET AL.: XCOM: Photon Cross Sections Database (1998), URL http://www.nist.gov/physlab/data/xcom/index.cfm, retrieved May 19th, 2010

[Bet30] BETHE, H.A.: Zur Theorie des Durchgangs schneller Korpuskularstrahlen durch Materie. *Ann. Phys.* (1930), vol. 397 Issue 3:pp. 325–400

[BN98] BECKER N., Wahrendorf J.: *Krebsatlas der Bundesrepublik Deutschland 1981-1990. Atlas of Cancer Mortality in the Federal Republic of Germany*, Springer, Berlin Heidelberg New York (1998), URL http://www.krebsatlas.de, updated online

[Bra05] BRAGG, W. H.: On the alpha particles of radium, and their loss of range in passing through various atoms and molecules. *Philosophical Magazine Series 6* (1905), vol. 10(57):pp. 318–340

[Dud72] DUDA, Richard O. and HART, Peter E.: Use of the Hough transformation to detect lines and curves in pictures. *Commun. ACM* (1972), vol. 15(1):pp. 11–15

[Fah09] FAHIMIAN, B.P.; DEMARCO, J.J.; KEYES, R.; BASSLER, N.; IWAMOTO, K.S.; ZANKL, M. and HOLZSCHEITER, M.H.: Antiproton radiotherapy: peripheral dose from secondary neutrons. *Hyperfine Interaction* (2009), vol. 194:pp. 313–318

[Fas05] FASSÒ, A.; FERRARI, A.; RANFT, J. and SALA, P.R.: FLUKA: A Multi-Particle Transport Code. *CERN-2005-10* (2005)

[Fre97] FREUND, Leopold: Ein mit Röntgenstrahlen behandelter Fall von Naevus pigmentosus piliferus. *Wiener Medizinische Wochenschrift* (1897)

[Fuj04] FUJIWARA, M. C.; AMORETTI, M.; BONOMI, G.; BOUCHTA, A.; BOWE, P. D.; CARRARO, C.; CESAR, C. L.; CHARLTON, M.; DOSER, M.; FILIPPINI, V.; FONTANA, A.; FUNAKOSHI, R.; GENOVA, P.; HANGST, J. S.; HAYANO, R. S.; JØRGENSEN, L. V.; LAGOMARSINO, V.; LANDUA, R.; LODI-RIZZINI, E.; MARCHESOTTI, M.;

MACRI, M.; MADSEN, N.; MANUZIO, G.; MONTAGNA, P.; RIEDLER, P.; ROTONDI, A. and ROULEAU, G.: Three-Dimensional Annihilation Imaging of Trapped Antiprotons. *Phys. Rev. Lett.* (2004), vol. 92(6):p. 065005

[Gue97] GUERRA, A. Del; DOMENICO, G. Di and MUKHOPADHAYAY, D.: PET dosimetry in proton radiotherapy: a Monte Carlo study. *Applied Radiation and Isotopes* (1997), vol. 48(10-12):pp. 1617–1624

[Hal06] HALL, Eric J.: *Radiobiology for the Radiologist*, Lippincott Williams & Wilkins (2006)

[Hig75] HIGHLAND, Virgil L.: Some practical remarks on multiple scattering. *Nuclear Instruments and Methods* (1975), vol. 129(2):pp. 497–499

[Hol06] HOLZSCHEITER, Michael H.; BASSLER, Niels; AGAZARYAN, Nzhde; BEYER, Gerd; BLACKMORE, Ewart; DEMARCO, John J.; DOSER, Michael; DURAND, Ralph E.; HARTLEY, Oliver; IWAMOTO, Keisuke S.; KNUDSEN, Helge V.; LANDUA, Rolf; MAGGIORE, Carl; MCBRIDE, William H.; MØLLER, Søren Pape; PETERSEN, Jørgen; SKARSGARD, Lloyd D.; SMATHERS, James B.; SOLBERG, Timothy D.; UGGERHØJ, Ulrik I.; VRANJES, Sanja; WITHERS, H. Rodney; WONG, Michelle and WOUTERS, Bradly G.: The biological effectiveness of antiproton irradiation. *Radiotherapy and Oncology* (2006), vol. 81(3):pp. 233–242

[Hou62] HOUGH, P.V.C.: Method and means for recognizing complex patterns (1962)

[Ino89] INOKUTI, Mitio: Interactions of antiprotons with atoms and molecules. *Nucl. Tracks. Radiat. Meas.* (1989), vol. 16:pp. 115–123

[Kal89] KALOGEROPOULOS, Theodore E. and MURATORE, Robert: Antiprotons for imaging and therapy. *NIMB* (1989), vol. 40-41(Part 2):pp. 1322–1325

[Kan10] KANTEMIRIS, I; ANGELOPOULOS, A; BASSLER, N; GIOKARIS, N; HOLZSCHEITER, M H; KARAISKOS, P; KALOGEROPOULOS, T E and THE AD-4/ACE COLLABORATION: Real-time imaging for dose evaluation during antiproton irradiation. *Phys. Med. Biol.* (2010), vol. 55:pp. N1–N9

[Kra00] KRAFT, Gerhard: Tumor Therapy With Heavy Charged Particles. *Prog. Part. Nucl. Phys.* (2000), vol. 45:pp. 473–544

[Lea46] LEA, D. E.: *Actions of Radiations on Living Cells*, Cambridge University Press, London (1946)

[Lyn91] LYNCH, Gerald R. and DAHL, Orin I.: Approximations to multiple Coulomb scattering. *Nuclear Instruments and Methods in Physics Research Section B: Beam Interactions with Materials and Atoms* (1991), vol. 58(1):pp. 6–10

[Nat] NATIONAL NUCLEAR DATA CENTER: Interactive Chart of Nuclides, online, URL http://www.nndc.bnl.gov/chart/, retrieved July 4th, 2010

[Par08] PARODI, Katia ET AL.: Comparison between in-beam and offline positron emission tomography imaging of proton and carbon ion therapeutic irradiation at synchrotron- and cyclotron-based facilities. *IJROBP* (2008), vol. 71(3):pp. 945–956

[Rie03] RIEDLER, Petra ET AL.: First results from the ALICE silicon pixel detector prototype. *NIMA* (2003), vol. A 501:pp. 111–118

[Rön95] RÖNTGEN, Wilhelm Conrad: Über eine neue Art von Strahlen. *Aus den Sitzungsberichten der Würzburger Physik.-medic. Gesellschaft 1895* (1895)

[Sch94] SCHOLZ, M. and KRAFT, G.: Calculation of Heavy Ion Inactivation Probabilities Based on Track Structure, X-ray sensitivity and target size. *Radiat. Prot. Dosimetry* (1994), vol. 52:pp. 29–33

[Sul85] SULLIVAN, A H: A measurement of the local energy deposition by antiprotons coming to rest in tissue-like material. *Phys. Med. Biol.* (1985), vol. 30:pp. 1297–1303

[Tes09] TESTA, E. ET AL.: Dose profile monitoring with carbon ions by means of prompt-gamma measurements. *NIMB* (2009), vol. 267:pp. 993–996

[The99] THE ALICE COLLABORATION: *ALICE Inner Tracking System (ITS): Technical Design Report*, Technical Design Report ALICE, CERN, Geneva (1999)

[WHO09] WHO: Fact Sheet No. 297: Cancer, online (2009), URL http://www.who.int/mediacentre/factsheets/fs297/en/

[Wil46] WILSON, Robert R.: Radiological Use of Fast Protons. *Radiology* (1946), vol. 47:pp. 487–491

[Wyl99] WYLLIE, Ken ET AL.: A pixel readout chip for tracking at ALICE and particle identification at LHCb. *5th Conference on Electronics for LHC Experiments* (1999):pp. 93–97

# Thanks!

I would like to thank all the people that supported me in the year of my diploma thesis.

- Professor Joachim Ullrich for the helpful questions and suggestions
- Michael Holzscheiter for the outstanding support and the almost 24/7 advice
- Oliver Jäkel for the quick and detailed help in any problem
- Carsten Welsch for the professional advice and the very constructive discussions
- My colleagues and friends within the QUASAR Group (especially Massimiliano), at the Max Planck Institute (Rebecca, Sara, Alexander, Marco), at DKFZ (Bernadette, Felix, Florian, Franz-Joachim, Gonzalo, Julia, Maria, Niels, Rochus, Steffen) for their useful comments, questions, and the cheerful time we have spent together
- The ALICE SPD group (Petra Riedler, Michele Caselle, Michel Morel, Vito Manzari, Michael Doser) for their great support and interest in this project
- My family: Brigitte, Peter, Sonja, Sebastian for their lifetime support and asking helpful questions in layman's terms
- My friends: Simone, Christian, Anna, Jens, Claudia, Max, Andreas, Friedrich
- and all the others which I have forgotten to mention.

# Vielen Dank Euch allen!

# Erklärung der Selbstständigkeit

Ich versichere, dass ich diese Arbeit selbstständig verfasst habe und keine anderen als die angegebenen Quellen und Hilfsmittel benutzt habe.

Heidelberg, den